

# Tajik Depression and Greater Pamir Neotectonics from InSAR Rate Maps

Sabrina Metzger<sup>1,1</sup>, Łukasz Gaęala<sup>2,2</sup>, Lothar Ratschbacher<sup>3,3</sup>, Milan Lazecky<sup>4,4</sup>, Yasser Maghsoudi<sup>4,4</sup>, and Bernd Dieter Schurr<sup>5,5</sup>

<sup>1</sup>Helmholtz-Zentrum, Deutsches GeoForschungsZentrum Potsdam

<sup>2</sup>Technische Universität Bergakademie Freiberg

<sup>3</sup>Geologie, Technische Universität Bergakademie Freiberg, 09599 Freiberg, Germany

<sup>4</sup>University of Leeds

<sup>5</sup>Deutsches GeoForschungsZentrum GFZ

November 30, 2022

## Abstract

Embedded between the Tian Shan, Pamir, and Hindu Kush, the Tajik depression is a remnant of the Mesozoic-Miocene Tajik-Tarim basin system. Since  $\sim 12$  Ma, westward collapse of the north-advancing Pamir-Plateau crust inverted the Tajik basin into a thin-skinned fold-thrust belt with  $\sim 150$  km of  $\sim$ E-W shortening distributed between foreland- and hinterland-vergent structures. Geodetically-derived shortening rates decay westward from  $\sim 15$  to 2 mm/yr. Seismicity outlines the  $\sim$ east-striking dextral Ilyak fault, bounding the fold-thrust belt in the north, and distributed shortening in the central and eastern Tajik depression. We derived E-W and vertical deformation-rate maps from radar interferometric time-series, consisting of 900+ radar scenes acquired over 2.0-4.5 years, and available accurate positioning data. We confirm the westward collapse of the Pamir and the drastic shortening-rate decline across the Main Pamir Thrust at the Pamir front. In the Tajik depression, the maps unveil a combination of basin-scale tectonics, local halokinesis, and seasonal/weather-driven soil or near-surface effects. Although the Tajik-basin strata move westward with rates decreasing away from the Pamir, the most external Babatag backthrust currently absorbs the highest shortening ( $\sim 6$  mm/yr) as it has done in the past ( $>20$  km). The Ilyak fault accommodates  $\sim 5-8$  mm/yr, eastward-increasing slip; rates decay sharply across the fault, suggesting a locking depth of  $<1$  km - possibly creep. At least 10 mm/yr uplift and westward motion occur across the Tajik-depression-Pamir transition, including the sinistral Darvaz fault zone, likely outlining a crustal-scale ramp. The Hoja Mumin salt fountain is spreading laterally at  $>300$  mm/yr.

## **Tajik Depression and Greater Pamir Neotectonics from InSAR Rate Maps**

**Sabrina Metzger<sup>1</sup>, Lukasz Gagala<sup>2,3</sup>, Lothar Ratschbacher<sup>2</sup>, Milan Lazecký<sup>4</sup>, Yasser Maghsoudi<sup>4</sup>, and Bernd Schurr<sup>1</sup>**

<sup>1</sup>Lithosphere Dynamics, Helmholtz Center, Research Center for Geosciences, Potsdam, Germany.

<sup>2</sup>Geologie, Technische Universität Bergakademie Freiberg, Freiberg, Germany.

<sup>3</sup>Now at Hellenic Petroleum, Marousi, Greece.

<sup>4</sup>COMET, School of Earth and Environment, University of Leeds, United Kingdom.

Corresponding author: Sabrina Metzger ([metzger@gfz-potsdam.de](mailto:metzger@gfz-potsdam.de))

### **Key Points:**

- East- and up-rate maps exhibit tectonic and anthropogenic processes with mm-accuracy in high spatial resolution (400 m)
- Rate map quality depends on interferometric data coherence and the availability of stabilizing GNSS data
- Major tectonic signal is E–W shortening in the Tajik fold-thrust belt due to the westward collapse of the Pamir-Plateau crust

## Abstract

Using E-W and vertical deformation-rate maps derived from radar interferometric time-series, we analyze the deformation field of an entire orogenic segment, i.e., the Tajik depression and its adjoining mountain belts, Tian Shan, Pamir, and Hindu Kush. The data-base consists of 900+ radar scenes acquired over 2.0–4.5 years and global navigation satellite system measurements. The recent, supra-regional kinematics is visualized in an unprecedented spatio-temporal resolution. We confirm the westward collapse of the Pamir-Plateau crust, inverting the Tajik basin into a fold-thrust belt with shortening rates decaying westward from  $\sim 15$  to 2 mm/yr. Vertical rates in the Hindu Kush likely record slab-dynamic effects, i.e., the progressive break-off of the Hindu Kush slab. At least 10 mm/yr of each, uplift and westward motion occur along the western edge of the Pamir Plateau, outlining the crustal-scale ramp along which the Pamir Plateau overrides the Tajik depression. The latter shows a combination of basin-scale tectonics, halokinesis, and seasonal/weather-driven near-surface effects. Abrupt  $\sim 6$  mm/yr horizontal-rate changes occur across the kinematically-linked dextral Ilyak strike-slip fault, bounding the Tajik fold-thrust belt to the north, and the Babatag backthrust, the major thrust of the fold-thrust belt, located far west in the belt. The sharp rate decay across the Ilyak fault indicates a locking depth of  $\leq 1$  km. The Hoja Mumin salt fountain is spreading laterally at  $\leq 350$  mm/yr. On the first-order, the modern 20–5 and fossil (since  $\sim 12$  Ma) 12–8 mm/yr shortening rates across the fold-thrust belt correspond.

## Plain Language Summary

The Tian-Shan-Pamir-Tibet-Himalaya mountain belts result from the Cenozoic collision of the Asian and Indian continents. Currently, the Pamir is colliding with the Tian Shan and collapsing westward into its foreland depression, creating the Tajik-basin fold-thrust belt. We use  $\sim 5$ -years of regularly acquired satellite radar imagery and pointwise positioning data to monitor the surface-deformation of the whole region. The resulting rate maps visualize crustal-scale tectonic and near-surface processes with an accuracy of a few millimeters and a spatial resolution of  $\sim 400$  m. The fold-thrust belt formed above a low-friction décollement, detached from the underlying basement, and terminates in the west and north along a kinematically-linked thrust–strike-slip fault system. In the eastern fold-thrust belt, salt rises forming a salt fountain that spreads up to 350 mm/yr. In agricultural areas, subsidence of  $> 10$  mm/yr is partially due to anthropogenically-caused water-level changes.

## 1. Introduction

At the western end of the India-Asian collision zone, the Tian Shan, Pamir, and Hindu Kush frame the Tajik depression, hosting the Tajik basin (Figure 1a). Deformation rates derived from pointwise Global Navigation Satellite System (GNSS) data along the northern and western margins of the Pamir reach  $\sim 20$  mm/yr (Metzger et al., 2020; Zubovich et al., 2010), being among the highest measured inside a continent. The accommodating crustal structures—thrusts and strike-slip faults—host abundant seismicity (e.g., Kufner et al., 2018; Schurr et al., 2014), including six magnitude M7 and eighteen M6.5 earthquakes during the past 115 years. All of these occurred in the center and along the northeastern and northwestern rims of the Pamir. Geologic, geophysical, and geodetic observations indicate that the Pamir has moved northward, building an orocline with 65–75-km-thick crust beneath the Pamir Plateau (Mechie et al., 2012;

Schneider et al., 2019). At the same time, the Pamir-Plateau crust has collapsed and has laterally (westward) extruded, thickening the crust west of the collision zone (Stübner et al., 2013; Rutte et al., 2017). Over the last ~12 Ma, westward extrusion into the Tajik depression has inverted the Tajik basin, forming the Tajik fold-thrust belt (FTB; Figures 1a and 1b; e.g., Abdulhameed et al., 2020; Gagała et al., 2020; Kufner et al., 2018; Nikolaev, 2002; Schurr et al., 2014; Stübner et al., 2013). Structural geometries, GNSS velocities, and seismicity inside the Tajik depression suggest that the Tajik FTB is thin-skinned, formed above an evaporitic décollement at 6–12 km depth (e.g., Bekker, 1996; Bourgeois et al., 1997; Gagała et al., 2020; Schurr et al., 2014). Although the distribution and age of deformation is known geologically, the relative short observation period used to record seismicity by high-resolution temporary networks (Kufner et al., 2018; Schurr et al., 2014), the sparse GNSS data (e.g., Ischuk et al., 2013; Metzger et al., 2020), and the paucity of detailed neotectonic observations (Trifonov, 1978) limit the quantification of how far the deformation field of the Pamir is influencing the Tajik depression and how the individual structures in the fold-thrust belt are contributing to its active shortening. In addition, the geodetically-derived rates might be influenced by salt tectonics (Ischuk et al., 2013; Metzger et al., 2020), anthropogenic effects (e.g., Mukhabbatov et al., 2020), disturbances by the recent large earthquakes (Metzger et al., 2020), and the mantle processes below the Hindu Kush and Pamir (Kufner et al., 2021, Sippl et al., 2013). Herein, we used a sampling method with high spatio-temporal resolution and large areal coverage— Interferometric Synthetic Aperture Radar (InSAR)—to assess the distribution of active deformation within the Tajik FTB and the surrounding mountain ranges.

Since the launch of the European Sentinel-1 radar satellite mission in 2014, Interferometric Synthetic Aperture Radar (InSAR) data have become easily accessible and tectonically active regions are monitored every 6–12 days worldwide. The data—usually provided in single tiles—cover  $\sim 240 \times 200$  km on ground (Figure 1c) and allow the detection of rate changes of  $\sim 1$  mm/yr (e.g., Weiss et al., 2020). Herein, we present relative displacement-rate maps derived from InSAR time-series analysis for the Tajik FTB and the adjoining Pamir and Hindu Kush with a spatial resolution of  $\sim 400$  m. We derive 13 individual rate maps in two independent view angles, tied to available GNSS rates in a Eurasia-fixed reference frame (Figure 1d), and decomposed into horizontal (E-W) and vertical rates (Figures 2 and 3).

Linking the rate maps to land-cover data, seismicity, and geologic structures formed over the last ~12 Ma, we observe and discuss the following first-order features: (1) In the Tajik and Ferghana depressions, the vertical rates outline stripes with  $>15$  mm/yr subsidence, with the strongest signal following the major river valleys; this subsidence is partially an artifact, partially caused by water extraction for irrigation. (2) In the Pamir, the horizontal rates outline a 3-D orogen-margin geometry with crustal material flowing laterally (westward) out of the N-S collision zone; the flow rates increase from east to west from the eastern to the western Pamir and decrease westward across the Tajik FTB, dissipating over its salt-rooted structures. (3) At the Tajik FTB's eastern edge and the adjacent western Pamir, high vertical and horizontal rates record passive roof uplift above a crustal-scale ramp, caused by the indentation of the leading

edge of the Pamir. (4) In the northern and western Tajik FTB, the kinematically-linked dextral Ilyak strike-slip fault and the Babatag thrust accommodate abrupt rate changes, marking the northern and western edge of the active Tajik FTB. (5) In the southeastern Tajik FTB, the rates trace active salt-tectonic structures. (6) In the Hindu Kush, large-wavelength displacement-rate changes likely record slab-dynamic processes in the mantle.

## 2. Tectonic Setting

The Tajik FTB and the bounding mountain belts of the Tian Shan, Pamir, and Hindu Kush formed due to the northward advance of the western promontory of India (e.g., Bloch et al., 2021b; Burtman & Molnar, 1993; Kufner et al., 2016; Schwab et al., 2004). Currently, the Pamir-Plateau crust moves northward, collides with the Tian Shan, and collapses and extrudes westward into the Tajik depression, forming the Tajik FTB (Figure 1a and 1b; Kufner et al., 2018; Schurr et al., 2014). The Tajik FTB comprises a series of westward-convex, ~N-trending folds and thrusts (e.g., Bourgeois et al., 1997; Chapman et al., 2017; Gaḡała et al., 2020) that bend in the north into the dextral Ilyak fault (Leith & Simpson, 1986); a similar—less pronounced—bending occurs in the south but no bounding strike-slip fault—akin to the Ilyak fault—has developed (Figures 2 and 3). The bending of the thrusts and folds into the Ilyak fault is compatible with the  $<50^\circ$ , paleomagnetically-determined, anti-clockwise vertical-axis rotations in the northern Tajik FTB (Pozzi & Feinberg, 1991; Thomas et al., 1994). The Tajik FTB, southwestern Tian Shan, and Hindu Kush reflect partitioning of the ~N4°E-oriented India-Asia convergence (DeMets et al., 1994) into ~N-S shortening accompanied by dextral slip in the Tian Shan and along the Ilyak fault, ~E-W shortening in the Tajik FTB, and ~NW-SE shortening in the Afghan platform in the foothills of the Hindu Kush (Käßner et al., 2016; Kufner et al., 2018; 2021; McNab et al., 2019).

Total ~E-W shortening reaches ~148 km in the north-central Tajik FTB, with decaying values towards south (~93 km) and towards northeast into the narrow corridor between the Pamir and Tian Shan (>22 km; Gaḡała et al., 2020). The southeastern part of the Tajik FTB showcases salt tectonics (Bekker, 1996; Gaḡała et al., 2020), e.g., at the Hoja Mumin salt fountain with vertical extrusion rates of ~170 mm/yr (Leith & Simpson, 1986). The southwestern Tian Shan—the Uzbek and Tajik Gissar—constitute the thick-skinned foreland buttresses to the Tajik FTB (Figure 1a; Gaḡała et al., 2020). To the east, along the front of the Pamir, the Tian Shan is separated from the Pamir Plateau by the Main Pamir Thrust System with its leading fault, the Pamir Frontal Thrust; the western part of the Pamir Frontal Thrust—in the Peter I. Range—is the dextral-transpressive Vakhsh thrust that transitions westward into the Ilyak fault (Figure 1a). In the Pamir, the ~NNW-striking, sinistral-transpressive Sarez-Karakul fault system separates the western and eastern Pamir (Figure 1a). The eastern Pamir is dominated by en-bloc northward advance, whereas the western Pamir has a distinct westward flow component (Ischuk et al., 2013; Kufner et al., 2018; Metzger et al., 2020).

Abdulhameed et al. (2020) estimated—based on low-temperature thermochronologic data that incorporate dates from Chapman et al. (2017) and Jepson et al. (2018)—that major

shortening started at ~12 Ma, spread immediately across the entire FTB, and declined at ~9 Ma in the western FTB; younger reactivation concentrated in the internal (eastern) FTB with the thickest evaporites. The youngest ages (~7–2 Ma) occur along the Vakhsh thrust, i.e., the active erosional front of the northeastern Tajik FTB belt, where it narrows between the converging Tian Shan and Pamir, and along the eastern edge of the FTB—at the western flank of the Pamir Plateau, dominated by the sinistral-transpressive Darvaz fault zone (Figure 1a). The onset of shortening at ~12 Ma yields 12–8 mm/yr average long-term shortening rates in the north-central and southern Tajik FTB (see total shortening values above).

GNSS survey profiles across the Pamir's northern and western margins provide insights into the large-scale deformation and fault kinematics (Figure 1b). The highest differential velocities are observed across the Pamir Frontal Thrust (13–19 mm/yr shortening, ~7 mm/yr dextral shear; Zubovich et al., 2010). Across the Vakhsh thrust, shortening is  $15 \pm 4/-2$  mm/yr, while dextral shear increases to  $16 \pm 3$  mm/yr; the Ilyak fault accommodates 8–15 mm/yr of dextral shear and ~5 mm/yr of shortening (Metzger et al., 2020). Kinematic modeling indicates a rather shallow fault-locking depth at the Vakhsh fault of <5 km (Metzger et al., 2020). The rates across the Darvaz fault zone decay from north to south, i.e., from ~15 to 7–9 mm/yr sinistral shear and from ~10 to 4–0 mm/yr extension. The Sarez-Karakul fault system accommodates  $5 \pm 2$  mm/yr sinistral slip (Metzger et al., 2017). The sparse GNSS data in the Tajik depression show that it is shortening ~ENE-WSW (Figure 1b; Ischuk et al., 2013; Metzger et al., 2020; Mohadjer et al., 2010). The interior of the Tian Shan exhibits minor dextral shear and shortening (Figure 1b). The recent kinematics of the Uzbek Gissar and the Afghan platform is largely unresolved. In the Hindu Kush, two relatively short GNSS profiles across the NE- to NNE-striking, poorly-mapped faults indicate sinistral-transpressive motion of  $\geq 2.5 \pm 1.8$  mm/yr in the central Hindu Kush and  $\geq 7.3 \pm 1.0$  mm/yr in the northeastern Hindu Kush (Badakhshan, Figures 1a and 1b; Kufner et al., 2021; Perry et al., 2018).

Abundant crustal seismicity highlights the most active faults, i.e., the Pamir Frontal Thrust, the Vakhsh thrust, the Darvaz fault zone, and the Sarez-Karakul fault system (Figures 1a and 1b; Kufner et al., 2018; Schurr et al., 2014; Sippl, et al., 2013). The earthquake focal mechanisms fit the observed fault kinematics (Figure 3; Kufner et al., 2018; Schurr et al., 2014). Seismicity is abundant beneath the Peter I. Range that is squeezed between converging Vakhsh and Darvaz faults, and north of the eastern Pamir, where the 2008  $M_w$ 6.6 Nura (Sippl et al., 2014; Teshebaeva et al., 2014; He et al., 2018) and the 2016  $M_w$ 6.4 Sary-Tash earthquakes (Bloch et al., 2021a; Funning & Garcia, 2019; Vajedian et al., 2017) ruptured the northern Main Pamir Thrust System, and the 2016  $M_w$ 6.6 Aketao/Muji earthquake (Wang et al., 2017; Feng et al., 2017) ruptured the Muji fault (Figure 1a). Sparse seismicity occurs in the western Tajik depression; in its eastern part, it is intense but diffuse with focal mechanisms indicating overall ~E-W shortening (Figure 3; Kufner et al., 2018). Most events occur at 5–25 km depth, i.e., in general below the evaporite décollement, with the overlying sedimentary stack deforming mostly aseismic (Gagała et al., 2020). The Ilyak fault appears to be mostly aseismic, apart from a cluster of seismicity southeast of Dushanbe (Figure 3; section 4.3.2.). In the Hindu Kush, crustal

seismicity is also sparse, suggesting that crustal faults are locked, with diffuse strain accumulation (Kufner et al., 2021).

In the context of our data analysis, a few large earthquakes stand out (Figure 1a): the 2015  $M_w$ 7.2 Sarez earthquake ruptured the central Pamir along the Sarez-Karakul fault system (Elliot et al., 2020; Metzger et al., 2017; Sangha et al., 2017); this event was in sequence with the two 2016  $M$ 6 earthquakes at the northern rim of the Pamir mentioned above (Bloch et al., 2021a). The 1949  $M_w$ 7.6 Khait earthquake likely affected the Tian Shan region north of Peter I. Range, causing a series of landslides (Evans et al., 2009; Kulikova, 2016). In 1907, the poorly located  $M_s$ 7.6  $\pm$  0.3 Kharatag earthquake occurred somewhere at the northern rim of the Tajik depression (Kondorskaya & Shebalin, 1982) or farther east in the Peter I. Range (Kulikova, 2016; Storchak et al., 2013). The Hindu Kush-Pamir region also hosts frequent intermediate-depth earthquakes at 80–300 km depth, which are related to the ongoing indentation of Indian cratonic lithosphere beneath the Pamir and the subduction and break-off of marginal Indian lithosphere below the central Hindu Kush (Figures 1a, 1b, 2a, and 2b; Sippl et al., 2013; Kufner et al., 2016, 2017, 2021). In 2015, during the InSAR data acquisition, the Hindu Kush hosted a  $M_w$ 7.5 earthquake at  $\sim$ 200 km depth, related to slab break-off (Kufner et al., 2017).

### 3. Data Processing

#### 3.1. InSAR Time-series Analysis

We used data from the Sentinel-1 satellites operating in C-Band with a wavelength of  $\sim$ 5.55 cm. The data were published as automatically pre-processed, differential interferograms as follows (Lazecký et al., 2020): each radar scene was automatically combined with three preceding and three subsequent scenes in time, resulting in six interferometric products with temporal baselines of a couple of weeks to months each (assuming no time gaps). The interferograms were created with the GAMMA SAR software (Wegmüller et al., 2016; Wegmüller & Werner, 1997) and multi-looked (downsampled) to  $\sim$ 100 m spatial resolution. They were filtered using an adaptive phase filter (Goldstein & Werner, 1998), assuming that short-baseline interferograms contain no sudden phase changes—e.g., due to fault creep—that are naturally smeared by strong filtering. Pixels with low coherence values were masked and the data were unwrapped automatically using SNAPHU v2 (Chen & Zebker, 2002). The unwrapped interferograms were resampled and geocoded using the 1-arc-second, void-filled digital elevation model of the Shuttle Radar Topography Mission (Farr et al., 2007). Each radar scene spatially overlaps along-track with other data frames of the same acquisition time and along-range with time-independent acquisitions (Figure 1c).

Interferometric time-series analysis allows to single out the small, secular tectonic and/or anthropogenic signals from the interferometric noise. This is done frame-wise (Figure 1c) by spanning a network of all interferometric scenes of one radar frame (Figure S1 of the supporting information). We used a modified small-baseline approach (NSBAS, Doin et al., 2011; López-Quiroz et al., 2009), as implemented in the python code LiCSBAS v1.3 (Morishita et al., 2020)

that directly integrates the above interferograms. Tropospheric noise was suppressed using synchronous tropospheric delay maps, which are based on extrapolated weather data of the European Centre for Medium-Range Weather Forecasts in a horizontal resolution of  $0.125^\circ$ , updated every six hours (Yu et al., 2018). We automatically excluded interferograms from further processing, if they contained sparse or noisy data or did not pass a phase-loop closure test (Biggs et al., 2007; De Zan et al., 2015) indicating severe unwrapping errors. The most stable pixel over time for each frame was selected as a reference pixel (red stars in Figures S2a and S2b). The whole interferometric network was then inverted for incremental displacements between the acquisition dates, with the mean (i.e., linear) displacement velocity being derived from the cumulative displacements by least-squares (Morishita et al., 2020). Network gaps were overcome by adding a linear constraint with a scaling factor to the Green's functions (Doin et al., 2011). The standard deviation of the inverted rates was obtained by percentile bootstrapping (Efron & Tibshirani, 1986). The uncertainties are usually underestimated, particularly if the network is not fully connected (Morishita et al., 2020; uncertainty investigations are discussed in section 4.1.). The resulting rate maps are masked by several quality assessment criteria, such as interferometric coherence, amount of data, rate standard deviation, time period covered, number of network gaps, or unwrapping errors, or root-mean-square of rate residuals. Finally, the maps were high-pass filtered in time and low-pass filtered in space using a Gaussian filter kernel (Hooper et al., 2007).

We processed six overlapping frames in ascending flight mode and seven frames in descending flight mode of three adjacent satellite tracks (Figure 1c). The assembled dataset covers  $270,000 \text{ km}^2$  in both view angles, stretching N–S from the Ferghana depression to the Hindu Kush and W–E from the Tajik depression to the eastern Pamir (Figure 2). When the mission's second satellite became fully operational at the end of 2016, the regular acquisition repeat time increased from 24 days to 12 days, which drastically increased the interferogram quality. In the Pamir, many frames show co- or post-seismic displacements related to the 2015  $M_w 7.2$  Sarez earthquake (Metzger et al., 2017; Fialko et al., 2021). In this region, we used only data acquired one year or more after the earthquake (Figure S1). Overall, each frame contains 255–500 interferograms of 82–175 radar images spanning 2–6 years (Table S1). To increase the processing speed, the interferograms were four-times multi-looked (i.e.,  $4 \times 4$  block complex-value averaged) to a ground resolution of  $\sim 350 \text{ m}$  in range and  $\sim 450 \text{ m}$  in azimuth. After quality assessment, the remaining 50–110 scenes spanned a network of 90–350 interferograms (Table S1). The rates resulting from the time-series analysis were masked using standard threshold parameters, i.e., an average coherence of  $>0.05$ , a rate standard deviation of  $<100 \text{ mm/yr}$ ,  $<10$  network gaps, and a spatio-temporal consistency of at least 5 mm. Some of these parameters were modified individually after visual inspection (Table S2). After the multi-looked and atmospheric-correction procedures, we repeated each processing step iteratively, removed poor interferograms, or corrected unwrapping errors manually. This improved the data quality, in particular in the rugged western Pamir, where the rates are most difficult to retrieve. The spatio-temporal filter was set to three times the average sampling interval in time and 2 km in space.

Topography-related phase signals were suppressed using a linear correction term estimated between 200 and 10,000 m elevation.

The completeness of the resulting rate maps correlates with topographic roughness (Figures S2a and S2b). While the Tajik depression and the arid eastern Pamir Plateau exhibit a relative high coverage, the deeply incised western Pamir, Tian Shan, and Hindu Kush are mostly void, apart from flat-bottom, formerly glaciated valleys (Stübner et al., 2017). The obtained deformation rates range between  $\pm 15$  mm/yr in line-of-sight (LOS) relative to their respective local reference points (Figures S2a and S2b). Due to data sparsity, the standard rate deviation of the descending frame 005D\_053 (Figure S2b) is significantly larger than those of the other frames; we excluded this frame from further processing. The rate uncertainties are between 0.5 and 3.0 mm/yr, with higher uncertainties in the descending acquisition geometry (Figure S3). The highest uncertainties are observed in the Panj valley in the western Pamir and south of the Hindu Kush, where either the topography or a poorly-resolved elevation model foster unwrapping errors. We excluded the area south of the Hindu Kush from further processing, as it also lacks stabilizing GNSS information. The lowest uncertainties are found near the reference points. These uncertainties only reflect a lower boundary, as they do not consider atmospheric disturbances or systematic biases caused by spatial subsampling and saw-blade like soil-moisture variations (see Figure 2 in Mira et al., 2021), which are problematic to correctly unwrap and cause bias in interferogram networks with short temporal baselines (Ansari et al., 2021; De Zan et al., 2014; Mathey et al., 2021), as we further discuss in section 4.3.1. Such biases can be suppressed to some extent if long-baseline interferograms are included in the interferometric network, and full resolution data are processed, which was not applicable in our case. However, we qualitatively estimated the spatial footprint of these biases by the phase-loop closure technique: for each frame, we calculated the mean of closed phase loops, that is, the sum of the interferometric phase difference  $\varphi_{ij} + \varphi_{jk} - \varphi_{ik}$ , between three acquisition epochs  $i$ ,  $j$ , and  $k$ , which is supposed to be zero (De Zan et al., 2015). If several of these loops are averaged, a systematic phase bias becomes apparent (Figure S4). For each frame, we calculated the sum of 70–90 phase loops acquired during 2017 to 2020. Significantly, mostly negative phase bias—correlated with the slow decrease of soil-moisture (see section 4.3.1.)—is observed in the Tajik and Ferghana depressions, and the extent of the affected regions is spatially well defined.

The outcome of our time-series analysis cannot only be used to derive linear rates, but also to monitor temporal rate anomalies, induced by seasonal processes (Figure S5 and S6), transients, or smaller earthquakes (see discussion in sections 4.2. and 4.3.2.). Thus, the noise level and temporal information in InSAR time-series nearly reach the one of daily GNSS time-series, but clearly outperform them in terms of spatial coverage.

### 3.2. Reference Frame and LOS Rate Decomposition

We collapsed all LOS rate maps with their individual stable reference points (Figures S2a and S2b) into a supra-regional Eurasia-fixed reference frame (Figures S2c and S2d), using published horizontal survey-mode GNSS data (Figure 1b; Ischuk et al., 2013; Kufner et al.,

2021; Metzger et al., 2019, 2020, 2021a; Mohadjer et al., 2010; Zubovich et al., 2016). During this first processing step, we identified and excluded four GNSS rates in the Tajik depression and one in the eastern Pamir as outliers (white arrows in Figure 2a; see also sensitivity tests in section 4.1.). Next, we tied each rate map into the Eurasia-fixed reference frame: we applied a linear ramp to each map to optimize (1) the fit to the horizontal GNSS rates within a search radius of  $\sim 4$  km (or 10 pixels), and (2) the along-track overlap of the data frames (Ou, 2020) by inverting an over-determined, weighted design matrix, where the GNSS rates were collapsed into LOS (more details are provided in the supporting information S1). After removal of the GNSS outliers, we added eight artificial data points (black squares in Figure 1d) to stabilize the frames covering the southern Hindu Kush, where GNSS data are sparse and which could not have been referenced otherwise. Their positions were placed at the edges of the respective radar frames, their rates were interpolated from the adjacent stations, and their uncertainties were doubled (gray arrows in Figure 1b). The individual rate maps of the descending tracks 078 and 005 were not fitted to match the along-track overlay, because the data in the overlap area were either too sparse or the deviation was abnormally large (Figure S2b; see also the sensitivity tests in section 4.1.). The resulting rates (Figures S2c and S2d) contain significant offsets across-track, which are mostly due to the sudden LOS change (Figure S7). The westward motion of the western Pamir dominates the ascending rate maps (Figure S2c) with positive values and the descending rate maps (Figure S2d) with negative values. Due to the right-looking acquisition geometry of the Sentinel-1 satellite, the data are sensitive to about 40, 10, and 50 % of the full east, north, and vertical displacement signals. If observations are available from ascending and descending LOS, they can be decomposed (Wright et al., 2004) into east and subvertical components by making use of the Pythagorean trigonometric identity between the LOS, east, and the subvertical direction (see sketch in Figure S8). The minor north component in the subvertical signal can be suppressed by subtracting interpolated north rates based on independent GNSS rates (Figure 1d; Ou, 2020; supporting information S1).

The resulting east rates agree with the corresponding GNSS data (Figure 2a) and range between -20 to +10 mm/yr in the ITRF2014 Eurasia-fixed reference frame (Altamimi et al., 2017). The vertical rates are in a data-centered reference frame and embrace  $\pm 18$  mm/yr (Figure 2b). The rates are most coherent in the Tajik and Ferghana depressions and—to some extent—in the eastern Pamir and the Alai valley. Rates in the western Pamir could only be extracted along the Panj-river valley and some of its tributaries. We still observe long-wavelength extrema at the corners and edges of some frames, e.g., in the NW-corner of frames 071A\_054 and 100A\_050 or the SW-corner of 078D\_052 (Figures 1c; markers “1” and “2” in Figure 2a). They are probably due to multiple unwrapping errors in disconnected, high-topography regions (Figures S2a and S2b). The spatial data coverage decreased further after decomposition (Figure S2) to regions covered by both view angles only. The decomposed rate uncertainties—now including the GNSS data uncertainties—are in the range of 0.6–2.6 mm/yr (Figures S9 and S10). In a similar study on Anatolia—with slightly more data—the uncertainties are in the range of 2–3 mm/yr for wavelengths of 50–150 km and a 5-year-long time-series (Figure S7 in Weiss et al., 2020). For

our slightly sparser dataset, we assume that local rate changes are significant if  $>1.5$  mm/yr, and long wavelength signals are significant if  $>3\text{--}5$  mm/yr. These estimates are probably still too optimistic for the Panj-river valley, where the interferometric networks are short in time and repeatedly sub-divided, impeding the correct assessment of linear rates (Figure S1), or where too few GNSS data points are available (Hindu Kush). There, the decomposed rate uncertainties are higher than in the rest of the dataset and reach 4.5 mm/yr. The individual ascending and descending rate maps and the final decomposed east and vertical rate maps, both stable to Eurasia (Altamimi et al., 2017) are available as geo-referenced TIF-files in Metzger et al. (2021b).

## 4. Results and Discussion

### 4.1. Rate Map Quality Assessment

Interferometric radar analysis is challenged by several factors. Seasonal vegetation changes and (ground) water dynamics introduce a bias, if only short temporal baseline interferograms are used (Figure S4; Ansari et al., 2021, Mathey et al., 2021), or if the network density is not equally distributed throughout the seasons. Heavy snowfall causes interferometric decorrelation, which may apply in particular for the western Pamir. The partially incomplete digital elevation model (Farr et al., 2007) of the deeply-incised western Pamir and southern Hindu Kush contains topographic artifacts, which makes interferograms prone to unwrapping errors. Given these obstacles, our LiCSBAS rate maps contain isolated data patches due to spatial and temporal decorrelation (Figure S2), which challenges the combination of the observed rates of several independent acquisition frames into one single reference frame. We overcame this to some extent by tying the rates to the GNSS reference frame, but some sharp jumps along frame boundaries remain; these are in the Afghan platform, the western Ferghana depression, the Dushanbe trough north of the Ilyak fault, and the upper Panj-river valley (markers “1” to “4” in Figure 2a, respectively). Also, the east rates of  $\sim 0$  mm/yr observed in the Muksu-river valley in the northern Pamir (Muksu in Figure 2a)—conflicting with the higher rates in the surrounding regions—are difficult to interpret. Thus, abundant GNSS data are fundamental to correctly transform LOS rate maps with spatial gaps into a supra-regional reference frame. For example, the sparse GNSS data in the Hindu Kush do not suffice to stabilize the observed, disconnected LOS rates correctly—particularly in the region south of the Hindu Kush—and we can only speculate if the long-wavelength signals are rooted in tectonics (Figures 2a and S2).

To further test the stability of the decomposed, Eurasian-fixed rate maps, we performed the steps described in section 3.2. three more times, using different referencing strategies. First, we included the five GNSS-rates identified and excluded as outliers in section 3.3.; then, we fitted also the along-track overlaps of frames 078 and 005, that originally exhibit a poor fit; finally, we combined the previous two procedures. A visual comparison of these tests shows that—apart from obvious sharp rate changes along frame boundaries—only long-wavelength patterns in the rate maps are affected (Figure S11). The inclusion of the GNSS-rate outliers

increases the westward motion of the region west of the Babatag fault by up to 4 mm/yr (models A in Figure S11), but introduces an obvious misfit between the InSAR and all other GNSS rates in the Tajik basin; it has no significant effect on the vertical rates. Fitting frames 078 and 005 along-track effects the southern Tajik basin strongest (models B in Figure S11), increasing the westward rate by 9 mm/yr and the subsidence by 8 mm/yr in the fold-thrust-belt; in the Hindu Kush, it yields unrealistic increase of east and uplift-rates by 13 and 6 mm/yr, respectively. Given the poor GNSS–InSAR misfit and the unrealistic rates for the Hindu Kush, we stick to the reference-frame strategy detailed in section 3.2.

The independent LiCSBAS rate maps offer reliable data to identify km-scale mass movements, which are abundant in this region, but these signals should be confirmed by optical imagery and/or fieldwork. We encourage the reader to make use of the supplementary material (Metzger et al., 2021b) for their own specific analyses. When interpreting our results, one must consider the different time periods of data collection (Figure S1). Each individual LOS rate map might be differently affected by moderate-sized earthquake signals or season-dependent near-surface dynamics. The Tajik depression yielded the highest data resolution in space and time, where we have both, dense data and distinct tectonic and non-tectonic signals that can be correlated with independent structural data in high-resolution. We therefore discuss the observations from the Pamir and Hindu Kush in a reconnaissance way and focus on the Tajik depression, in particular the Tajik FTB.

#### 4.2. Pamir and Hindu Kush

In the Eurasia-fixed reference frame, the InSAR rates exhibit westward motion in the order of  $\geq 10$  mm/yr in the western Pamir and the Tajik FTB with a good match to the GNSS-derived east rates (Figure 2a). We assign the large-scale west-directed surface displacements to the westward collapse and lateral extrusion of the Pamir-Plateau crust. North of the Pamir-Tian Shan collision boundary, the Ferghana depression appears to lack horizontal motion (i.e., it is relatively stable in reference to Eurasia), as all significant features in the rate maps also appear in the phase-bias map (Figure S4) or collocate with radar-frame boundaries (marker “2” in Figure 2a) and hence are artifacts. Along the northern front of the Pamir in the southern Alai valley (Figures 1a, 2a, and 2c), sharp rate changes record the westward-increasing dextral shear at the leading edge of the Pamir, indicating its escape towards the west in addition to the dominant N–S shortening showcased by GNSS data (Zubovich et al., 2010, 2016). The east-rate map also indicates that part of the active deformation steps back south of the eastern Alai valley from the Pamir Frontal Thrust and connects to the  $\sim$ WNW-striking Muji fault (Figures 1a, 2a, and 2c). It remains indistinguishable whether the recorded velocities reflect post-seismic activation following the 2016 Sary-Tash and Muji earthquakes (Bie et al., 2018; Feng et al., 2017) or are a long-term signal. Afterslip can be excluded, since we removed data acquired in (at least) the first six months after these two M6 events, but a slight non-linear signal is still observable in individual time-series (e.g., Figures S6g to S6j). In any case, the indicated rates support the transfer of the top-to-west normal slip along the Kongur Shan extensional system of the eastern

Pamir (e.g., Robinson et al., 2004; 2007; just outside and southeast of the eastern boundary of Figure 2a) via the Muji fault and the Kyzilart transfer zone (marker “a” in Figure 2a) to the Pamir Thrust System and in particular to the deformation front along the Pamir Frontal Thrust (Sippl et al., 2014). The existence of this dextral transfer zone, consisting of the Muji fault and the faults of the Kyzilart transfer zone, that transfer ~E-W crustal extension along the Kongur Shan system to the dextral strike-slip component along the Pamir front, is also implied by the slight divergence of the GNSS velocity field between the eastern Pamir (e.g., Lake Karakul area in Figure 2a) and the Tarim block (Zubovich et al., 2010). North of the transfer zone the GNSS vectors parallel those in the Tarim basin, albeit with lower rates than in the Tarim basin, reflecting the shortening across the multiple faults of the Pamir Thrust System (Figures 2a and 2c). The dextral transfer zone (Muji fault and faults of the Kyzilart transfer zone) implies that the eastern Pamir is involved in the partitioning of convergence into ~N-S shortening and ~E-W extension, here with a westward flow component smaller than that of the western Pamir.

At the northwestern rim of the Pamir, along the Vakhsh valley, sharp east-rate changes of 12–24 mm/yr either imply high landslide activity or—more likely—a shallow locking depth of the evaporite-rooted, dextral-transpressive Vakhsh thrust (Figures 2a and 2d); the estimated dextral strike-slip rates are  $16 \pm 3$  mm/yr (Metzger et al., 2020). If the Vakhsh thrust is nearly freely creeping, the 1949  $M_w$ 7.6 Khait earthquake likely did not rupture the Vakhsh thrust but a structure in the crystalline basement of the Tian Shan.

On first order—and given that the east rates measured in the valleys of the Panj and its tributaries are significant, the west rates appear to increase from 5–15 mm/yr westward motion in the eastern Pamir (east of the Sarez-Karakul fault system) to 15–20 mm/yr in the western Pamir; this conforms with the intense western Pamir seismicity with focal mechanisms that show strike-slip and normal fault solutions with ~E-trending T-axes (Schurr et al., 2014). A minor westward rate increase occurs across the distributed segments of the Sarez-Karakul fault system, e.g., near Lake Sarez (Figures 1a and 2a). The implied extensional deformation component accommodated by the Sarez-Karakul fault system agrees with the geologic observations of major range-bounding normal faults northeast of Lake Sarez (Officers Range, marker “OR” in Figure 2a; Rutte et al., 2017; Schurr et al., 2014) but contrasts with focal mechanism solutions, which record nearly pure sinistral strike-slip (Metzger et al., 2017; Schurr et al., 2014). However, we consider the rates in this area somewhat uncertain, as some short wavelength rate changes correlate with slopes and the systematic bias map (Figure S4). We suspect that this is not a topographic artifact but rather caused by seasonal, permafrost-related sagging of (or pore-pressure changes in) unconsolidated material (e.g., Rouyet et al., 2019); we extensively mapped such features that formed as a result of the 2015 Sarez earthquake (the light-blue lines in Figures 2a and 2b show the modeled rupture trace from Metzger et al., 2017).

The northeastern Hindu Kush of Badakhshan (Figure 1a), with reliable data along the Kokcha-river valley (marker “b” in Figure 2a), exhibits nearly as high westward rates (7–12 mm/yr) as the eastern Tajik FTB (8–15 mm/yr) and the western Pamir (marker “c” in Figure 2a,

16–26 mm/yr). No modern structural information is available for the faults and folds mapped in the northeastern Hindu Kush, but the highest rate changes coincide with thrust-cored folds along the southeastern margin of the Tajik FTB, involving Pliocene strata (Figure 3a; Doebrich & Wahl, 2006; own unpublished mapping). In contrast, the western Hindu Kush—including the Afghan platform—appears to be horizontally mostly stable with respect to Eurasia (west of marker “b” in Figure 2a,  $0 \pm 2$  mm/yr).

We observe strong and accelerating uplift of 10–17 mm/yr in the westernmost Pamir (along the Panj valley and west of it) and easternmost Tajik FTB where its eastern erosional edge is cut by the Darvaz fault zone (marker “d” in Figures 2b and 3b, time-series in Figures S5a and S5b); this area coincides with the area of rapid westward motion (marker “c” in Figure 2a; see interpretation below). The acceleration started  $\sim 1$  yr (Figure S5a and S5b) after the Sarez and the slab-break-off earthquakes 200–250 km farther east and south, respectively (Figures 1a, 2a, and 2b).

A N–S gradient—with uplift rates of 4–6 mm/yr—occurs at the southern margin of the Tajik depression at its transition to the Afghan platform (marker “e” in Figure 2b). This area south of the Amu Darya–Panj-river valley, marks the interaction and transition from the  $\sim$ E–W shortening of the Tajik FTB to the  $\sim$ NW–SE shortening within the Afghan platform, implied by earthquake focal mechanism (e.g., Supplementary Figure S5 in Kufner et al., 2021; McNab et al., 2019), and the appearance of  $\sim$ E-striking faults, e.g., the dextral-oblique thrust in the Alburz–Marmul fault zone (Figure 1a).

The whole northeastern Hindu Kush and southwestern Pamir are located above steeply-dipping lithospheric slabs; their position in the mantle is outlined by depth contours of intermediate-depth seismicity in Figure 1a and the intermediate-depth earthquake epicenters in Figures 1b, 2a, and 2b (e.g., Kufner et al., 2016, 2017, 2021; Zhan & Kanamori, 2016). The Pamir slab starts to bend down from west to east beneath the eastern Tajik FTB (Figures 6 and 7 in Schneider et al., 2019; crustal-scale cross section in Figure 18c of Gaglia et al., 2020) and likely laterally terminates in the south where strong uplift (marker “d” in Figure 2b) gives way to subsidence in the northeastern Hindu Kush (marker “f” in Figure 2b). The Hindu Kush slab is subducting northward, dips steeply north to vertical, and is in the process of stretching and tearing in its eastern part (Kufner et al., 2017, 2021). The boundary between the mantle parts of the two slabs is outlined by the intermediate-depth earthquakes in the southwestern-most Pamir (Hindu Kush slab: purple dots; Pamir slab: pink dots in Figures 2a and 2b). It is difficult to assess, whether these deep-seated processes are reflected in our rate maps. InSAR radar satellite antennas are most sensitive to vertical motions, but subtle rate changes across several tens—if not hundreds of kilometers—are challenging to correctly retrieve. Our observation of clearly linear, regional, 0–4 mm/yr subsidence in the northeastern Hindu Kush (marker “f” in Figure 2b; Figure S5i) above and north of the Hindu Kush slab, and in particular the marked contrast to the 10–17 mm/yr uplift in the easternmost Tajik FTB (marker “d” in Figure 2b) likely record these lithosphere processes. This regional subsidence remains—or even increases—despite the

different reference framing strategies discussed in section 4.1. (Figure S11). The region where the crust of the Tajik depression bends down, forming the footwall of the western Pamir (crustal-scale buckling in profile along latitude 38°N in Figure 6 of Schneider et al., 2019; Gaḡala et al., 2020), likely constitutes a crustal-scale antiform above a ramp, causing uplift. In the southwestern Pamir, the steeply ~SE-dipping to vertical, back-rolling Pamir slab (Kufner et al., 2016) possibly induces subsidence (Figure 2b). The north-dipping to subvertical, back-rolling Hindu Kush slab possibly induces the subsidence in the Hindu Kush (marker “f” in Figure 2b): there, subsidence of up to 4 mm/yr changes to uplift at the western end of the slab where it is intact (boundary between markers “e” and “f”) and subsidence possibly changes to modest uplift at the slab’s eastern end, where the break-off has progressed most (Kufner et al., 2021). We interpret the general  $\geq 10$  mm/yr subsidence south of marker “f” and south of the eastern part of marker “e” as a tectonic signal caused by the Hindu Kush slab; there, Kufner et al. (2021) tomographically mapped its down-bending towards a subvertical position in the mantle marked by the purple earthquakes. In contrast to these long-wavelength features, we interpret the pronounced stripes of 20–40 mm/yr subsidence crossing and extending to the south of marker “e” along the Kunduz-river valley as anthropogenically-caused (Figure 2b; see section 4.3.1. for equivalent subsidence along the valleys of the Tajik depression).

#### 4.3. Active Structures in the Tajik Fold-thrust Belt

The rates in the Tajik FTB are interpreted in combination with seismicity (Kufner et al., 2018) and the structural geometries, derived from surface, seismic, and borehole data (Gaḡala et al., 2020). In addition to the map view (Figure 3), we projected the horizontal and vertical rates onto four geologic cross-sections within 5 km swaths (Figures 4a and 4b; cross-section traces in Figure 3), and into a detailed east-rate map and an oblique-crossing profile of the Ilyak fault (Figure 5; frame in Figure 3a). In addition, we compared the rates to topographic profiles and percentage of arable land, both computed within 5 km swaths (Figures 4a and 4b).

##### 4.3.1. Non-tectonic Signal

Herein, we outline the non-tectonic signal, that is systematic subsidence, by land classification data based on Landsat 8 optical imagery (MDA US BaseVue, 2013); land classified as arable correlates well with the systematic soil-moisture bias map (Figure S4). We marked the major agricultural areas by polygons framed thick-white (Figure 3b) respectively shaded in green (Figures 4a and 4b). The vertical rate maps of Figures 2b and 3b outline stripes with  $>15$  mm/yr subsidence as the most outstanding feature of the Tajik depression; the strongest subsidence signal follows the major river valleys of the Tajik depression, which host intense agriculture. The observed subsidence is most likely caused by precipitation-induced soil-moisture changes that alter the dielectric properties and thus the vertical propagation of the incoming radar waves (Ansari et al., 2021; De Zan et al., 2014). Rainfall and/or snowmelt causes rapid pore filling and simultaneous soil uplift (Gabriel et al., 1989), which often leads to unwrapping errors in interferograms. The consequent slow dehumidification (see Figure 2 in Mira et al., 2021), on the other hand, is correctly imaged in interferograms, thus biasing the

vertical rates derived from the time-series analysis towards the negative. This bias is likely strongly enhanced by water extraction due to the extensive irrigation in the summer months, during which most of the used radar scenes were acquired; a more detailed study of these signals lies beyond the scope of this work. In the horizontal rates, the agricultural areas often coincide with a high measurement scatter, although without any systematic component. A second conspicuous vertical signal—but this time positive—correlates with major rivers and related to water level increase during hinterland snow melt (e.g., markers “g” in Figure 3b).

The distinct, patchy subsidence in the region between the fossil and active (Hoja Mumin) salt diapirs in the southeastern Tajik FTB and the Nurak water reservoir (markers “HM” and “NR” in Figure 2b) are likely an effect of salt tectonics (Figure 11 of Gaḡala et al., 2020). But it is also correlating with arable land that has not been properly classified in the Landsat 8 data. The highest deformation rates occur at the Hoja Mumin salt fountain (Figure 2e), where we observed local uplift of ~50 mm/yr at its top, surrounded by up to ~120 mm/yr of subsidence and lateral outflow of ~350 mm/yr to the west and ~170 mm/yr to the east. These rates confirm the recent activity of this salt fountain, as documented by Leith & Simpson (1986), Dooley et al. (2015), and Gaḡala et al. (2020). We also observed localized uplift surrounding the shores of the Nurak reservoirs (and smaller reservoirs downstream; marker “NR” in Figure 2b and cross-sections A and B in Figure 4a) that is probably related to elastic rebound caused by reservoir-volume changes, as it was confirmed elsewhere (e.g., Cavalié et al., 2007; Neelmeijer et al., 2018).

#### 4.3.2. Tectonic Signal

The unambiguous horizontal tectonic signal consists of long-wavelength trends. Foremost, the bulk of the Tajik FTB accommodates westward motion (map view in Figures 2a and 3a, cross-sectional view in Figures 4a and 4b). Characteristically, the east rates are not affected by the vergence of the fold-thrust structures in the Tajik FTB; in particular, the Yavan synclinorium—the zone of vergence change—is showing similar horizontal rates as the bounding Kafirnigan and Vakhsh anticlinoria. Therefore, the Yavan synclinorium must be—at least at present—entirely detached from its original substratum. Chapman et al. (2017) postulated that the east-vergent western Tajik FTB is part of the greater Tian Shan orogenic system, distinct from the eastern Tajik FTB whose shortening is linked to the Pamir, with the Yavan synclinorium being a remnant foreland common to both fold-thrust systems; again—at least at present—the west-directed rates indicate the detachment of the entire Tajik FTB as part of the outward-growing Pamir orogenic system.

The west-directed rates decay away from the Pamir: Figure 3a shows—in average—higher westward displacements in the part of the Tajik FTB adjacent to the Pamir than away from it. Cross-sections A, B and C in Figures 4a and 4b illustrate this pattern (envelope ‘A’ in the horizontal displacement profiles), while in the southernmost cross-section D this trend is not convincing. We interpret this decrease by the gradual dissipation of the west-directed motion across the FTB-internal, salt-rooted thrusts and folds; however, this absorption of displacement

by FTB-internal structures is subordinate to the coherent westward displacement of the whole Tajik FTB. The rates decrease and become less systematic towards south (cross-sections A–C versus D; Figures 4a and 4b), suggesting active, northward-increasing, anti-clockwise vertical-axis rotations in the Tajik FTB, in agreement with the sense of past rotations evidenced by paleomagnetic data (Pozzi & Feinberg, 1991; Thomas et al., 1994).

In detail, the horizontal displacement profiles often show a saw-blade pattern (Figures 4a and 4b). These short-wavelength perturbations stand out across the Kafirnigan anticlinorium, where positive spikes—reaching up to 10 mm/yr above the regional background—are centered over scarp slopes of east-facing hogback ridges (“E” markers placed over the horizontal displacement profiles in cross-section B and C; Figures 4a and 4b). Figure 6a highlights these short-wavelength anomalies in a high-pass filtered map of horizontal rates that suppresses the regional component: the east-facing scarp slopes (“E” markers) show narrow but pronounced positive, the west-facing slopes negative, albeit less pronounced horizontal displacement anomalies. The divisions between the local positive and negative anomalies follow the crests of the topographic ridges, suggesting divergent ground motions across the ridge crests. We interpret the short-wavelength saw-blade patterns—superimposed on the regional displacement profiles—as related to gravitationally-induced mass movements (slope sagging or creep) and rule out topographic artifacts, as these perturbations also vary along elevation isolines. Due to the homoclinal structure of the hogback ridges in the Kafirnigan anticlinorium, the east-facing scarp slopes incise older strata, including mass-movement prone Cenomanian-Campanian shale, marl, limestone, and evaporites, while the west-facing ones follow in general sandstone- and conglomerate-dominated Oligocene-Neogene strata with less mass-movement susceptibility; this likely causes the faster ground motion on eastern than western slopes. Figure 6b provides structural evidence for northwest-directed mass movement, albeit without age control: along a steeply west-dipping slope in the ~NW-dipping strata of the Karshi anticline—east of the Babatag anticline, an Upper Cretaceous shale-gypsum sequence shows dominantly ~NW-directed normal faulting, with the fault planes, shear zones, and numerous tension gashes infiltrated/lubricated by gypsum.

Across the frontal anticline of the Vakhsh anticlinorium, where the hogback ridges face west due to the change of the structural polarity across the Yavan synclinorium, this relationship seems to be reversed: there, the west-facing scarp slopes (“W” markers in cross-sections B and C of Figures 4a and 4b; Figure 6a) correlate with negative displacement spikes. This indicates that a local west-directed displacement component adds up to the regional displacement. We propose the same explanation as for the Kafirnigan anticlinorium, i.e., variable susceptibility of the slopes to mass movements; however, the relationship is more diffuse in the Vakhsh than in the Kafirnigan anticlinorium, possibly due to the complex surface geology, in particular the presence of incised hanging-wall anticlines.

An abrupt ~5 mm/yr change in the east rates occurs across the Ilyak fault and the Babatag thrust (Figures 2a, 3a, 4a, and 5). The Babatag thrust accommodates an abrupt arrest of the Tajik

FTB's westward motion. It is the most prominent structure of the Tajik FTB in terms of the amount of shortening with total displacement exceeding 20 km over the past ~12 Ma in its northern segment; total displacement drops to ~10 km in the south (Gagała et al., 2020). The horizontal velocity contrast across this thrust is ~5 mm/yr all along strike, although the velocity gradient in the north (cross-sections B and C; Figures 4a and 4b) is higher than in the south (cross-section D). The absolute numbers indicate a passive hanging wall and actively underthrusting footwall. The dip of the Babatag thrust—constrained by boreholes—is ~15° (Gagała et al., 2020), hence, the horizontal underthrusting at ~5 mm/yr should resolve in ~1.3 mm/yr vertical displacement of the hanging wall; such an uplift anomaly is not evident, probably due to its low value compared to the noise. Recent activity of the Babatag thrust may independently be indicated by geomorphology: Figure S12 shows a series of 500-m-wide swath profiles along selected stream trunks. Most of the profiles display knickpoints, possibly indicating topographic perturbations due to slip along the Babatag thrust; the most affected stream profiles (2, 3, 5 in Figure S12) face an exposed portion of the Babatag thrust where it overrides Quaternary alluvia. However, due to the resolution of the current-state of geologic mapping in this area (scale 1:200,000), we cannot assess the effect of lithological changes on the position of the knickpoints in detail.

Cross-section A in Figure 4a shows and Figure 5 details the transition of the Tajik FTB to the Dushanbe trough, which is involved in the moderate ~N–S shortening of the Tian Shan to the north (Käbner et al., 2016; Gagała et al., 2020). Figure 5 shows the structures, seismicity, and east-rate changes across the Ilyak fault southeast of Dushanbe, where the fault exhibits a horizontal rate change within a corridor of  $\leq 4$  km. In an elastic screw dislocation model, 50 % of the fault's relative motion should occur in a corridor of twice its locking depth (Savage & Burford, 1973); this would suggest that the fault is locked at  $< 1$  km depth, if not—given the spatial sampling of ~350, respectively ~450 m and the strong filtering of the original interferograms—freely creeping as suggested by InSAR LOS rate maps produced by higher spatial sampling (Wilkinson et al., 2020). Dextral slip varies along strike and decreases from ~10 mm/yr in the east to ~5 mm/yr in the west (Figures 5a and 5b). Seismicity is sparse except for an area ~20-km west of Dushanbe, where the focal mechanisms suggest dextral shear (Figure 5a; Kufner et al., 2018). This is where the fault changes strike and several thrusts of the Kafirnigan anticlinorium enter the Ilyak fault, forming transpressive shear lenses, imbricating Lower Cretaceous to Pliocene rocks.

We have no direct structural information on the Ilyak fault, mostly due its strong anthropogenic overprint. The data at the three sites shown in Figure 5c characterize the northern edge of the Dushanbe trough and the Vakhsh anticlinorium south and north of the Ilyak fault, respectively. Pure top-to-south thrusting emplaced the crystalline basement of the Tian Shan on Cretaceous limestone of the Tajik basin at station 1893A at the northern rim of the Dushanbe trough; the age of thrusting is unknown but younger than ~10 Ma (Käbner et al., 2016). The lack of a strike-slip signal confirms that the band of westward displacement signal, coinciding with a series of thrusts farther east, is a radar frame artifact (marker “3” in Figures 2a and 5a). The

~NE-striking fault east of Dushanbe, well-expressed topographically and forming a clear boundary between agricultural and pastoral land, appears to accommodate west-directed rates of up to 5 mm/yr, highlighting FTB-internal deformation. The two sites (Figure 5c) in the Vakhsh anticlinorium south of the Ilyak fault characterize that part of the Tajik FTB where the overall ~N-striking thrusts progressively bend into the Ilyak fault zone. Characteristically, the thrusts have dextral-transpressive top-to-(N)NW kinematics; these faults accommodate horizontal rate changes of a few mm/yr. Our data neither support nor disprove the hypothesis that the 1907  $M_s 7.6 \pm 0.3$  Kharatag earthquake occurred on a locked fault ~100 km west of Dushanbe (Figure 1a; Kondorskaya & Shebalin, 1982).

An obvious but small active structure is a ~N-striking fault south of the conjunction of Vakhsh, Panj, and Kunduz rivers that exhibits frequent seismicity and where the hanging wall exhibits increased west-directed motion (marker “h” in Figures 3a and 3b). Its surface trace reaches a length of ~15 km but may be connected with a similar structure north of the Amu Darya, also hosting a cluster of seismicity and two focal mechanism solutions that indicate slip along ~N-striking sub-horizontal planes (Kufner et al., 2018). The original time-series of a pixel selected in the hanging wall captured about ~3 cm of slip towards ascending LOS after a 2017, January 9,  $M_w 5.2$  earthquake (event 201701090559A, Ekström et al., 2012; Figure S5j). Our kinematic observations agree with the double couple solution from the Global Centroid Moment Tensor catalog that reports thrusting on a ~46°-dipping plane on a ~SSE-striking fault (marked in orange and labeled by magnitude; Figure 3). The epicenter, however, is ~15 km west of the cluster of earthquakes (Kufner et al., 2018). We consider the structure to be part of the southernmost Kafirnigan anticlinorium, where it bends from a ~N to a ~SE strike, marking the southern margin of the Tajik FTB.

Extremely rapid westward motion occurs west of the Darvaz fault zone, at the eastern erosional edge of the Tajik FTB, where westward rates reach 16–26 mm/yr (marker “c” in Figures 2a and 2e; markers “I” in Figure 4a); these high rates can be observed from the Peter I. Range in the north all the way to west of the Kokcha river in Badakhshan in the south, interrupted by a relatively stable area and with only locally retrievable signal along the Panj valley. Vertical uplift rates also increase towards the Darvaz fault reaching 10–17 mm/yr (marker “d” in Figure 2b; envelopes B in Figures 4a and 4b; see section 4.2.). The area of rapid uplift coincides with high topography, developed in often weakly-consolidated Neogene coarse-grained terrestrial strata (Figure 4, topographic swath profiles). From our uncertainty analyses (Figures S3, S4, S8, S10, and S11), we can exclude atmospheric or near-surface contributions to these rates, thus they are of tectonic origin. Both the high horizontal rates and the Pamir-ward—probably temporarily—increase of the vertical uplift rates support the earlier given interpretation (section 4.2.) of a tectonic stack above a ramp, caused by ongoing indentation of the leading edge of the Pamir below this marginal part of the Tajik depression, resulting in a passive roof uplift; the temporary increase possibly correlates in time with the  $M_w 7.2/7.5$  Sarez/slab break-off earthquakes (Figure S5a and S5b). The rapid westward motion and the uplift, however, appear inconsistent with the modern sinistral kinematics of the Darvaz fault (Kufner et al., 2018);

Metzger et al., 2020). We favor an interpretation of slip partitioning, with top-to-WNW thrusting of the Pamir's buried leading edge being kinematically decoupled by the sinistral Darvaz fault from the Pamir hinterland. We envision a similar displacement partitioning as described for the deformation at the northern edge of the Pamir, east of the Alai valley (section 4.2.): there, dominant northward motion is accommodated by the large thrusts of the Pamir Thrust System (with the recent Nura and Sary-Tash earthquakes) and subordinate dextral strike-slip faults, the Muji fault and the Kyzilart transfer zone (with the recent Muji earthquake), that accommodate the westward escape of the Pamir. In this scenario, the thrusts and strike-slip faults at the eastern edge of the Tajik FTB would partition deformation in northward motion along the Darvaz fault zone (and little-studied parallel faults in the western Pamir of Badakhshan) and westward motion along the thrusts.

If significant, the westward increase of the horizontal rates west of the Darvaz fault zone (marker “c” in Figures 2a and 2e) would imply ongoing extension along the eastern border of the displacement anomaly and concomitant shortening along its western border, a pattern typical for gravity-driven deformation. Past extension is indeed evidenced by likely Neogene graben fills in the Darvaz fault zone (Figure 2e; Gagała et al., 2020), but we are lacking structural and geomorphic data to confirm that such a process is operating today. We interpret the eastern edge of the Tajik FTB as the western margin of the province with strike-slip and normal fault focal mechanisms that indicate ~E–W extension across the western Pamir (Schurr et al., 2014). The westward increasing rates may indicate the zone where the crust of the topographically-high western Pamir Plateau acquires a component of westward gravitational sliding being transferred from the crustal ramp to the salt-décollement of the Tajik FTB.

There is a conspicuous westward horizontal rate increase of up to 7 mm/yr across a ~NNE-trending watershed between the Panj and the Kokcha rivers that seems to be a true kinematic signal (marker “j” in Figures 2a, 2e, and 3a); towards east, rates increase again to ~8 mm/a westward movement (southern extension of marker “c” in Figures 2a and 2e), which we interpreted above as due to a component of westward gravitation sliding along the western margin of the Pamir Plateau. The boundary of increased westward motion at marker “j” coincides with the transition from the west-vergent thrust-folds with thick Neogene hanging-wall strata to the area in the southeastern Tajik FTB that is governed by salt-tectonics (marker “H” in cross-section D of Figure 4b). The box-shaped antiform with a >25-km wavelength, cored by up to 5-km-thick evaporites and a salt diapir at its western tip west of marker “H”, may indicate a zone of enhanced westward flow feeding the various thrust detachment folds with thick evaporite cores farther west. This indicates that parts of the buried salt structures of the southeastern Tajik FTB—besides the Hoja Mumin salt fountain—are active; the strong anthropogenic overprint prohibits an interpretation of the vertical displacements but as in the area between the Nurak reservoir and Hoja Mumin salt fountain, the subsidence signal features a distinct, patchy pattern.

## 5. Conclusions

Our research shows that interferometric rate-map creation for an entire orogenic segment is challenging given the extreme changes in—for example—topography, precipitation, and vegetation. Aided by the high velocities at the western margin of the India-Asia collision zone, our rate maps offer insights into the horizontal and vertical displacement field that pointwise sampling methods (e.g., GNSS) cannot provide. Combined with seismicity and—in particular—geologic and thermochronologic data, it provides an efficient approach to integrate the short- and long-term rate observations into a detailed orogenic evolution.

The interferometric rate maps of the greater Pamir area exhibit large-scale tectonic features, ground subsidence due to water level changes, salt tectonics, and mass movements. Rate interpretation is limited by data sparsity of the underlying interferometric network in time and space. Single interferograms of poor quality—containing unwrapping errors across disconnected regions, for example—might significantly influence the 13 derived relative rate maps in LOS. The Global Navigation Satellite System (GNSS) data play a key role to correctly tie the rate maps to a supra-regional, Eurasian-fixed reference frame and the decomposition of the LOS rates into east and vertical rates, particularly for long-wavelength signals. Our GNSS data quality is somewhat limited, as the database contains only horizontal rates, derived from repeated, annual surveys in difficult terrain and confined by topography. The temporal resolution and accuracy of spatio-temporally filtered InSAR time-series (in line-of-sight) nearly equals daily GNSS solutions and are able to reproduce ephemeral and seasonal processes. We discussed the most conspicuous tectonic and anthropogenic features, and linked them to the seismicity, and the geologic structures formed over the last ~12 Ma.

The displacement-rate maps highlight the 3-D geometry of large parts of the northwestern orogenic margin of the India-Asia collision zone, with crustal material flowing laterally (westward) out of the N-S convergence zone. The west-directed lateral extrusion rates increase from east to west from the eastern to the western Pamir and decrease from ~20 to 5 mm/yr westward across the Tajik fold-thrust belt (Tajik FTB), dissipating over the salt-rooted structures. On the first-order, the modern shortening rates across the Tajik fold-thrust belt (20–5 mm/yr) correspond to the 12–8 mm/yr long-term shortening rates (148–93 km shortening over 12 Myr) in the north-central and southern Tajik fold-thrust belt, determined from line-length restoration and thermochronology. Characteristically, the modern westward rates are not affected by the vergence of the Tajik fold-thrust belt structures, in particular the Yavan synclinorium—the zone of vergence change; therefore, the entire Tajik fold-thrust belt is detached from its original substratum. The modern kinematics thus shows that the Tajik fold-thrust belt is a depression-wide, thin-skinned belt developed above an evaporitic décollement, whose evolution is governed by the westward growth of the Pamir orocline. A short-wavelength saw-blade pattern—superimposed on the regional horizontal displacement profiles—is interpreted as related to mass movements on steeply-dipping slopes of structurally controlled hogback ridges.

Abrupt  $\sim 6$  mm/yr changes in the horizontal rates occur across the kinematically-linked dextral Ilyak strike-slip fault bounding the Tajik fold-thrust belt to the north and the Babatag thrust, the major thrust of the fold-thrust belt, located far west in the belt. The dextral slip or creep rates on the Ilyak fault are of 5–10 mm/yr, decreasing towards west; the locking depth of the fault is  $\leq 1$  km.

The vertical and horizontal rates of the southeastern Tajik fold-thrust belt are laterally diverse with a distinct, patchy displacement signal, in particular in the region with salt tectonics, where upright detachment anticlines and bivergent thrust sheets pointing at an unconfined detachment. The highest velocities occur at the Hoja Mumin salt fountain, where we observed local uplift of  $\sim 50$  mm/yr at its top, surrounded by up to  $\sim 120$  mm/yr of subsidence and lateral outflow of  $\sim 350$  mm/yr to the west and  $\sim 170$  mm/yr to the east.

The vertical rate map outlines stripes with  $>15$  mm/yr subsidence as the most outstanding feature of the Tajik depression; the strongest subsidence signal follows the major river valleys of the Tajik depression, which host intense agriculture. The subsidence is caused by a combination of a bias related to soil-moisture changes (slow dehumidification) and probably water extraction for the extensive irrigation. In addition, we observed strong uplift of 10–17 mm/yr in the western Pamir and the easternmost Tajik FTB where its eastern erosional edge is cut by the broad Darvaz fault zone. Both the high horizontal rates and the Pamir-ward increase of the vertical uplift rates support the existence of a crustal-scale antiform above a ramp caused by ongoing indentation of the leading edge of the Pamir below this marginal part of the Tajik depression, resulting in a passive roof uplift.

Further interferometric rate studies of high relevance in the Tajik FTB could address the anthropogenic impact on the vertical rates and detail the recent activity in a classic salt-tectonic province. The provided rate maps should be a starting point for this research.

## **Acknowledgments**

Qi Ou advised us on how to tie multiple InSAR rate maps to GNSS data. Some figures were created using GMT (Wessel et al., 2013) and fair data-representation colormaps (Cramer, 2020). LiCS interferograms (Looking into the Continents from Space, <https://comet.nerc.ac.uk/comet-lics-portal/>) contain modified Copernicus Sentinel data analyzed by COMET, the Centre for the Observation and Modelling of Earthquakes, Volcanoes and Tectonics, using JASMIN, the UK's collaborative data analysis environment (<http://jasmin.ac.uk>). Atmospheric phase delay maps were provided by the Generic Atmospheric Correction Online Service for InSAR (<http://www.gacos.net>). GNSS rate tables are published as mentioned in the text. The individual and the final, decomposed rate maps and uncertainties are provided in Metzger et al. (2021b). Funded by the Helmholtz Center, German Research Center for Geosciences, Potsdam, the German Research Council (DFG) grant RA 442/40, and the German Ministry of Science and Education within the CaTeNA project (support 3G0878A). We thank Rishav Mallick and an anonymous reviewer for their suggestions on how to improve the manuscript.

## References

- Abdulhameed, S., Ratschbacher, L., Jonckheere, R., Gagała, Ł., Enkelmann, E., Käßner, A., et al. (2020). Tajik Basin and Southwestern Tian Shan, Northwestern India-Asia Collision Zone: 2. Timing of Basin Inversion, Tian Shan Mountain Building, and Relation to Pamir-Plateau Advance and Deep India-Asia Indentation. *Tectonics*, 39(5), e2019TC005873 <https://doi.org/10.1029/2019TC005873>
- Altamimi, Z., Métivier, L., Rebischung, P., Rouby, H., & Collilieux, X. (2017). ITRF2014 plate motion model. *Geophysical Journal International*, 209(3), 1906–1912. <https://doi.org/10.1093/gji/ggx136>
- Ansari, H., De Zan, F., & Parizzi, A. (2021). Study of Systematic Bias in Measuring Surface Deformation with SAR Interferometry. *IEEE Transactions on Geoscience and Remote Sensing*, 59(2), 1285–1301. <https://doi.org/10.1109/TGRS.2020.3003421>
- Bekker, Y.A. (1996). Tectonics of the Afghan–Tadjik Depression (russ.), *Geotektonika*, 30(1), 76–82.
- Biggs, J., Wright, T., Lu, Z., & Parsons, B. (2007). Multi-interferogram method for measuring interseismic deformation: Denali Fault, Alaska, *Geophysical Journal International*, 170(3), 1165–1179. <https://doi.org/10.1111/j.1365-246X.2007.03415.x>
- Bie, L., Hicks, S., Garth, T., Gonzalez, P., & Rietbrock, A. (2018). ‘Two go together’: Near-simultaneous moment release of two asperities during the 2016  $M_w$  6.6 Muji, China earthquake, *Earth and Planetary Science Letters*, 491, 34–42. <https://doi.org/10.1016/j.epsl.2018.03.033>
- Bloch, W., Metzger, S., Schurr, B., Yuan, X., Ratschbacher, L., Reuter, S., Xu, Q., Zhao, J., Murodkulov, Sh., & Oimuhhammadzoda, I. (2021a). The 2015–2017 Pamir Earthquake Sequence: Fore-, Main-, and Aftershocks, Seismotectonics and Fault Interaction, *Earth and Space Science Open Archive*, preprint published on Oct 20, 2021. <https://doi.org/10.1002/essoar.10508392.1>
- Bloch, W., Schurr, B., Yuan, X., Ratschbacher, L., Reuter, S., Kufner, S-K., Xu, Q., & Zhao, J. (2021b). Structure and stress field of the lithosphere between Pamir and Tarim, *Geophysical Research Letters*, <https://doi.org/10.1029/2021GL095413>.
- Bourgeois, O., Cobbold, P. R., Rouby, D., Thomas, J.-C., & Shein, V. (1997). Least squares restoration of Tertiary thrust sheets in map view, Tajik depression, central Asia, *Journal of Geophysical Research*, 102(B12), 27553–27573. <https://doi.org/10.1029/97JB02477>
- Burtman, V. S., & Molnar, P. (1993). Geological and Geophysical Evidence for Deep Subduction of Continental Crust Beneath the Pamir. *Geological Society of America Special Paper*, 281, 1–76. <https://doi.org/10.1130/SPE281>
- Cavalié, O., Doin, M.-P., Lasserre, C., & Briole, P. (2007). Ground motion measurement in the Lake Mead area, Nevada, by differential synthetic aperture radar interferometry time series analysis: Probing the lithosphere rheological structure, *Journal of Geophysical Research: Solid Earth*, 112(B3), 1–18. <https://doi.org/10.1029/2006JB004344>
- Chapman, J. B., Carrapa, B., Ballato, P., DeCelles, P. G., Worthington, J., Oimahmadov, I., Gadoev, M., Ketcham, R. (2017). Intracontinental subduction beneath the Pamir

- Mountains: Constraints from thermokinematic modeling of shortening in the Tajik fold-and-thrust belt, *GSA Bulletin*, 129(11–12), 1450–1471. <https://doi.org/10.1130/B31730.1>
- Chen, C. W., & Zebker, H. A. (2002). Phase unwrapping for large SAR interferograms: Statistical segmentation and generalized network models, *IEEE Transactions on Geoscience and Remote Sensing*, 40(8), 1709–1719. <https://doi.org/10.1109/TGRS.2002.802453>
- Crameri, F. (2020). Scientific color maps (Version 6.0.4). <https://doi.org/10.5281/zenodo.4153113>
- DeMets, C., Gordon, R. G., Argus, D. F., & Stein, S. (1994). Effect of recent revisions to the geomagnetic reversal time scale on estimates of current plate motions, *Geophysical Research Letters*, 21(20), 2191–2194. <https://doi.org/10.1029/94GL02118>
- De Zan, F., Parizzi, A., Prats-Iraola, P., & López-Dekker, P. (2014). A SAR interferometric model for soil moisture, *IEEE Transactions on Geoscience and Remote Sensing*, 52(1), 418–425. <https://doi.org/10.1109/TGRS.2013.2241069>
- De Zan, F., Zonno, M., & López-Dekker, P. (2015). Phase Inconsistencies and Multiple Scattering in SAR Interferometry, *IEEE Transactions on Geoscience and Remote Sensing*, 53(12), 6608–6616. <https://doi.org/10.1109/TGRS.2015.2444431>
- Doeblich, J. L., & Wahl R. R. (Compilers) (2006). Geological and mineral resource map of Afghanistan; Version 2. *U.S. Geol. Surv. Open File Rep.*, 2006–1038.
- Doin, M.-P., Lodge, F., Guillaso, S., Jolivet, R., Lasserre, C., Ducret, G., et al. (2011). Presentation of the small baseline NSBAS processing chain on a case example: the Etna deformation monitoring from 2003 to 2010 using Envisat data, *Proceedings of the ESA Fringe 2011 Workshop*, Frascati, Italy, 19–23.
- Dooley, T. P., Jackson, M. P. A., & Hudec, M. R. (2015). Breakout of squeezed stocks: Dispersal of roof fragments, source of extrusive salt and interaction with regional thrust faults, *Basin Research*, 27(1), 3–25. <https://doi.org/10.1111/bre.12056>
- Efron, B., & Tibshirani, R. (1986). Bootstrap Methods for Standard Errors, Confidence Intervals, and Other Measures of Statistical Accuracy, *Statistical Science*, 1, 54–75. <https://doi.org/10.1214/ss/1177013815>
- Ekström, G., Nettles, M., & Dziewonski, A. M. (2012). The global CMT project 2004–2010: Centroid-moment tensors for 13,017 earthquakes, *Physics of the Earth and Planetary Interiors*, 200–201, 1–9. <https://doi.org/10.1016/j.pepi.2012.04.002>
- Elliott, A., Elliott, J., Hollingsworth, J., Kulikova, G., Parsons, B., & Walker, R. (2020). Satellite imaging of the 2015 M7.2 earthquake in the Central Pamir, Tajikistan, elucidates a sequence of shallow strike-slip ruptures of the Sarez-Karakul fault, *Geophysical Journal International*, 221(3), 1696–1718. <https://doi.org/10.1093/gji/ggaa090>
- Evans, S. G., Roberts, N. J., Ischuk, A., Delaney, K. B., Morozova, G. S., & Tutubalina, O. (2009). Landslides triggered by the 1949 Khait earthquake, Tajikistan, and associated loss of life, *Engineering Geology*, 109(3–4), 195–212. <https://doi.org/10.1016/j.enggeo.2009.08.007>

- Farr, T. G., Rosen, P. A., Caro, E., Crippen, R., Duren, R., Hensley, S., et al. (2007). The Shuttle Radar Topography Mission, *Review of Geophysics*, 45(RG2004), 248.  
<https://doi.org/10.1029/2005RG000183>
- Feng, W., Tian, Y., Zhang, Y., Samsonov, S., Almeida, R., & Liu, P. (2017). A Slip Gap of the 2016 M<sub>w</sub>6.6 Muji, Xinjiang, China, Earthquake Inferred from Sentinel-1 TOPS Interferometry. *Seismological Research Letters*, 88(4), 1054–1064.  
<https://doi.org/10.1785/0220170019>
- Fialko, Y., Jin, Z., Zubovich, A., & Schöne, T. (2021). Lithospheric deformation due to the 2015 M7.2 Sarez (Pamir) earthquake constrained by 5 years of space geodetic observations, *Earth and Space Science Open Archive*, preprint published on Oct 1, 2021.  
<https://doi.org/10.1002/essoar.10508106.1>
- Funning, G. J., Garcia, A. (2019). A systematic study of earthquake detectability using Sentinel-1 Interferometric Wide-Swath data, *Geophysical Journal International*, 216(1), 332–349, Figure S23 in the supporting information. <https://doi.org/10.1093/gji/ggy426>
- Gabriel, A. K., Goldstein, R. M., and Zebker, H. A. (1989). Mapping small elevation changes over large areas: Differential radar interferometry, *Journal Geophysical Research*, 94(B7), 9183– 9191. <https://doi.org/10.1029/JB094iB07p09183>
- Gagała, Ł., Ratschbacher, L., Ringenbach, J. C., Kufner, S.-K., Schurr, B., Dedow, R., et al. (2020). Tajik Basin and Southwestern Tian Shan, Northwestern India-Asia Collision Zone: 1. Structure, Kinematics, and Salt Tectonics in the Tajik Fold-and-Thrust Belt of the Western Foreland of the Pamir, *Tectonics*, 39(5), e2019TC005871.  
<https://doi.org/10.1029/2019TC005871>
- Goldstein, R. M., & Werner, C. L. (1998). Radar interferogram filtering for geophysical applications, *Geophysical Research Letters*, 25(21), 4035–4038.  
<https://doi.org/10.1029/1998GL900033>
- He, P., Hetland, E. A., Niemi, N.A., Wang, Q., Wen, Y. and Ding, K. (2018). The 2016 Mw6.5 Nura earthquake in the Trans Alai range, northern Pamir: possible rupture on a back-thrust fault constrained by Sentinel-1A radar interferometry, *Tectonophysics*, 749, 62–71.  
<https://doi.org/10.1016/j.tecto.2018.10.025>
- Hooper, A., Segall, P., & Zebker, H. (2007). Persistent scatterer interferometric synthetic aperture radar for crustal deformation analysis, with application to Volcán Alcedo, Galápagos, *Journal of Geophysical Research: Solid Earth*, 112(7), 1–21.  
<https://doi.org/10.1029/2006JB004763>
- Ischuk, A., Bendick, R., Rybin, A., Molnar, P., Khan, S. F., Kuzikov, S., et al. (2013). Kinematics of the Pamir and Hindu Kush regions from GPS geodesy, *Journal of Geophysical Research: Solid Earth*, 118(5), 2408–2416.  
<https://doi.org/10.1002/jgrb.50185>
- Jepson, G., Glorie, S., Konopelko, D., Gillespie, J., Danišik, M., Evans, N. J., et al. (2018). Thermochronological insights into the structural contact between the Tian Shan and Pamirs, Tajikistan, *Terra Nova*, 30, 95–104. <https://doi.org/10.1111/ter.12313>
- Käbner, A., Ratschbacher, L., Jonckheere, R., Enkelmann, E., Khan, J., Sonntag, B.-L., et al. (2016). Cenozoic intracontinental deformation and exhumation at the northwestern tip of

- the India-Asia collision—southwestern Tian Shan, Tajikistan, and Kyrgyzstan, *Tectonics*, 35(9), 2171–2194. <https://doi.org/10.1002/2015TC003897>
- Kondorskaya, N., & Shebalin, N. (chief editors). (1982). New Catalog of Strong Earthquakes in the U.S.S.R. from Ancient Times Through 1977, Report SE31, *World Data Center A for Solid Earth Geophysics*, 609.
- Kufner, S.-K., Schurr, B., Sippl, C., Yuan, X., Ratschbacher, L., son of Mohammad Akbar, A., et al. (2016). Deep India meets deep Asia: Lithospheric indentation, delamination and break-off under Pamir and Hindu Kush (Central Asia), *Earth and Planetary Science Letters*, 435, 171–184. <https://doi.org/10.1016/j.epsl.2015.11.046>
- Kufner, S.-K., Schurr, B., Haberland, C., Zhang, Y., Saul, J., Ischuk, A., & Oimahmadov, I. (2017). Zooming into the Hindu Kush slab break-off: a rare glimpse on the terminal stage of subduction, *Earth and Planetary Science Letters*, 461, 127–140. <https://doi.org/10.1016/j.epsl.2016.12.043>
- Kufner, S.-K., Schurr, B., Ratschbacher, L., Murodkulov, S., Abdulhameed, S., Ischuk, A., et al. (2018). Seismotectonics of the Tajik Basin and Surrounding Mountain Ranges, *Tectonics*, 37(8), 2404–2424. <https://doi.org/10.1029/2017TC004812>
- Kufner, S.-K., Kakar, N., Bezada, M., Bloch, W., Metzger, S., Yuan, X., et al. (2021). The Hindu Kush slab break-off as revealed by deep structure and crustal deformation, *Nature Communications*, 12, 1685. <https://doi.org/10.1038/s41467-021-21760-w>
- Kulikova, G. (2016). Source parameters of the major historical earthquakes in the Tien-Shan region from the late 19th to the early 20th century, *PhD Thesis*, Potsdam University
- Lazecký, M., Spaans, K., González, P. J., Maghsoudi, Y., Morishita, Y., Albino, F., et al. (2020). LiCSAR: An automatic InSAR tool for measuring and monitoring tectonic and volcanic activity, *Remote Sensing*, 12(15). <https://doi.org/10.3390/RS12152430>
- López-Quiroz, P., Doin, M.-P., Tupin, F., Briole, P., & Nicolas, J. M. (2009). Time series analysis of Mexico City subsidence constrained by radar interferometry, *Journal of Applied Geophysics*, 69, 1–15. <https://doi.org/10.1016/j.jappgeo.2009.02.006>
- Leith, W., & Simpson, D. W. (1986). Earthquakes related to active salt doming near Kulyab, Tadzhikistan, USSR, *Geophysical Research Letters*, 13(10), 1019–1022. <https://doi.org/10.1029/GL013i010p01019>
- Mathey, M., Doin, M.-P., André, P., Walpersdorf, A., Baize, S., & Sue, C. (2021), Spatial Heterogeneity of Uplift Pattern in the Western European Alps Revealed by InSAR Time Series Analysis, *accepted to Geophysical Research Letters*, <https://doi.org/10.1029/2021GL095744R>, preprint available at *Earth and Space Science Open Archive*, <https://doi.org/10.1002/essoar.10507009.1>
- McNab, F., Sloan, R. A., & Walker, R. T. (2019). Simultaneous orthogonal shortening in the Afghan-Tajik Depression, *Geology*, 47(9), 862–866. <https://doi.org/10.1130/G46090.1>
- Mechie, J., Yuan, X., Schurr, B., Schneider, F., Sippl, C., Ratschbacher, L., et al. (2012). Crustal and uppermost mantle velocity structure along a profile across the Pamir and southern Tien Shan as derived from project TIPAGE wide-angle seismic data, *Geophysical*

- Journal International*, 188(2), 385–407. <https://doi.org/10.1111/j.1365-246X.2011.05278.x>
- [Mira, N. C., Catalão, J., Nico, G., & Mateus, P. \(2021\). Soil Moisture Estimation Using Atmospherically Corrected C-Band InSAR Data. \*IEEE Transactions on Geoscience and Remote Sensing\*. <https://doi.org/10.1109/TGRS.2021.3109450>](#)
- Metzger, S., Schurr, B., Ratschbacher, L., Sudhaus, H., Kufner, S.-K., Schöne, T., et al. (2017). The 2015  $M_w$ 7.2 Sarez strike-slip earthquake in the Pamir interior: Response to the underthrusting of India's western promontory, *Tectonics*, 36(11), 2407–2421. <https://doi.org/10.1002/2017TC004581R>
- Metzger, S., Ischuk, A., Akhmedov, A., Ilyasova, Z., Moreno, M., Murodkulov, S., & Deng, Z. (2019). Survey mode GPS data in the West Pamir, Tajikistan, Central Asia, 2013–2016, *GFZ Data Services*. <https://doi.org/10.5880/GFZ.4.1.2019.007>
- Metzger, S., Ischuk, A., Deng, Z., Ratschbacher, L., Perry, M., Kufner, S.-K., et al. (2020). Dense GNSS profiles across the northwestern tip of the India-Asia collision zone: Triggered slip and westward flow of the Peter the First Range, Pamir, into the Tajik depression, *Tectonics*, 39(2), e2019TC005797. <https://doi.org/10.1029/2019TC005797>
- Metzger, S., Kakar, N., Zubovich, A., Borisov, M., Saif, S., Panjsheri, A. H., Rahmani, J. R., Zaryab, M. Y., Rezai, M. T., Deng, Z., Bendick, R., Kufner, S.-K., & Okoev, J. (2021a). Survey mode GNSS data, acquired 2014–2019 in the Afghan Hindu Kush and across northern Pamir margin, Central Asia, *GFZ Data Services*. <https://doi.org/10.5880/GFZ.4.1.2021.003>
- [Metzger, S., Lazecký, M., & Maghsoudi, Y. \(2021\). High-resolution rate maps from the Tajik basin and the Pamir. \*GFZ Data Services\*. <https://doi.org/10.5880/GFZ.4.1.2021.005>](#)
- Mohadjer, S., Bendick, R., Ischuk, A., Kuzikov, S., Kostuk, A., Saydullaev, U., et al. (2010). Partitioning of India-Eurasia convergence in the Pamir-Hindu Kush from GPS measurements, *Geophysical Research Letters*, 37(4). <https://doi.org/10.1029/2009GL041737>
- Morishita, Y., Lazecky, M., Wright, T. J., Weiss, J. R., Elliott, J. R., & Hooper, A. (2020). LiCSBAS: An Open-Source InSAR Time Series Analysis Package Integrated with the LiCSAR Automated Sentinel-1 InSAR Processor, *Remote Sensing*, 12(3), 5–8. <https://doi.org/10.3390/rs12030424>
- [Mukhabbatov, H. M., Zhiltsov, S. S., & Markova, E. A. \(2020\). Tajikistan water resources and water management issues. In: Zonn, I.S., Zhiltsov, S.S., Kostianoy, A.G., & Semenov, A.V \(eds.\), \*Water Resources Management in Ventral Asia\*, \*Hdb. Env. Chem.\*, 105, 111–124. \[https://doi.10.1007/698\\\_2020\\\_602\]\(https://doi.10.1007/698\_2020\_602\)](#)
- Neelmeijer, J., Schöne, T., Dill, R., Klemann, V., & Motagh, M. (2018). Ground Deformations around the Toktogul Reservoir, Kyrgyzstan, from Envisat ASAR and Sentinel-1 Data—A Case Study about the Impact of Atmospheric Corrections on InSAR Time Series, *Remote Sensing*, 10(3), 462. <https://doi.org/10.3390/rs10030462>
- Nikolaev, V. G. (2002). Afghan-Tajik depression: Architecture of sedimentary cover and evolution, *Russian Journal of Earth Science*, 4(6), 399–421.

- Ou, Q. (2020). Crustal strain and seismic hazard of the NE Tibetan Plateau, *PhD Thesis*, University of Oxford. <https://ora.ox.ac.uk/objects/uuid:139c5ffd-5f50-4ca8-b56f-39da3c91d914>
- Perry, M., Kakar, N., Ischuk, A., Metzger, S., Bendick, R., Molnar, P., & Mohadjer, S. (2018). Little Geodetic Evidence for Localized Indian Subduction in the Pamir-Hindu Kush of Central Asia, *Geophysical Research Letters*, *46*(1), 109–118. <https://doi.org/10.1029/2018GL080065>
- Pozzi, J. P., & Feinberg, H. (1991). Paleomagnetism in the Tajikistan: Continental shortening of European margin in the Pamirs during Indian Eurasian collision, *Earth and Planetary Science Letters*, *103*(1–4), 365–378. [https://doi.org/10.1016/0012-821X\(91\)90173-F](https://doi.org/10.1016/0012-821X(91)90173-F)
- Robinson, A. C., Yin, A., Manning, C. E., Harrison, T. M., Zhang, S.-H., Wang, X.-F. (2004). Tectonic evolution of the northeastern Pamir: Constraints from the northern portion of the Cenozoic Kongur Shan extensional system, western China, *GSA Bulletin*, *116*(7–8), 953–973. <https://doi.org/10.1130/B25375.1>
- Robinson, A. C., Yin, A., Manning, C. E., Harrison, T. M., Zhang, S.-H., Wang, X.-F. (2007). Cenozoic evolution of the eastern Pamir: Implications for strain-accommodation mechanisms at the western end of the Himalayan-Tibetan orogen, *GSA Bulletin*, *119*(7–8), 882–896. <https://doi.org/10.1130/B25981.1>
- Rouyet, L., Lauknes, T. R., Christiansen, H. H., Strand, S. M., & Larsen, Y. (2019). Seasonal dynamics of a permafrost landscape, Adventdalen, Svalbard, investigated by InSAR, *Remote Sensing of Environment*, *231*, 111236. <https://doi.org/10.1016/j.rse.2019.111236>
- Rutte, D., Ratschbacher, L., Schneider, S., Stübner, K., Stearns, M. A., Gulzar, M. A., et al. (2017). Building the Pamir-Tibetan Plateau – Crustal stacking, extensional collapse, and lateral extrusion in the Central Pamir: 1. Geometry and kinematics, *Tectonics*, *36*(3), 342–384. <https://doi.org/10.1002/2016TC004293>
- Sangha, S., Peltzer, G., Zhang, A., Meng, L., Lian, C., Lundgren, P., et al. (2017). Fault geometry of 2015, Mw7.2 Murghab, Tajikistan earthquake controls rupture propagation: Insights from InSAR and seismological data, *Earth and Planetary Science Letters*, *462*, 132–141. <https://doi.org/10.1016/j.epsl.2017.01.018>
- Savage, J. C., & Burford, R. O. (1973). Geodetic Determination of Relative Plate Motion in Central California, *Journal of Geophysical Research*, *78*(5), 832–845. <https://doi.org/10.1029/JB078i005p00832>
- Schneider, F. M., Yuan, X., Schurr, B., Mechie, J., Sippl, C., Kufner, S.-K., et al. (2019). The Crust in the Pamir: Insights from Receiver Functions, *Journal of Geophysical Research: Solid Earth*, *124*, 9313–9331. <https://doi.org/10.1029/2019JB017765>
- Schurr, B., Ratschbacher, L., Sippl, C., Gloaguen, R., Yuan, X., & Mechie, J. (2014). Seismotectonics of the Pamir, *Tectonics*, *33*(80), 1501–1518. <https://doi.org/10.1002/2014TC003576>
- Schwab, M., Ratschbacher, L., Siebel, W., McWilliams, M., Minaev, V., Lutkov, V., et al. (2004). Assembly of the Pamirs: Age and origin of magmatic belts from the southern Tien Shan to the southern Pamirs and their relation to Tibet, *Tectonics*, *23*, TC4002. <https://doi.org/10.1029/2003TC001583>

- Sippl, C., Schurr, B., Yuan, X., Mechie, J., Schneider, F. M., Gadoev, M., et al. (2013). Geometry of the Pamir-Hindu Kush intermediate-depth earthquake zone from local seismic data, *Journal of Geophysical Research: Solid Earth*, *118*(4), 1438–1457. <https://doi.org/10.1002/jgrb.50128>
- Sippl, C., Ratschbacher, L., Schurr, B., Krumbiegel, C., Rui, H., Pingren, L., & Abdybachaev, U. (2014). The 2008 Nura earthquake sequence at the Pamir-Tian Shan collision zone, southern Kyrgyzstan, *Tectonics*, *33*(12), 2382–2399. <https://doi.org/10.1002/2014TC003705>
- Sperner, B. & Ratschbacher, L. (1994). A Turbo Pascal program package for graphical presentation and stress analysis of calcite deformation, *Zeitschriften der Deutschen Geologischen Gesellschaft*, *145*, 414–423.
- Storchak, D. A., Di Giacomo, D., Bondár, I., Engdahl, E. R., Harris, J., Lee, W. H. K., et al. (2013). Public release of the ISC-GEM global instrumental earthquake catalogue (1900–2009), *Seismological Research Letters*, *84*, 810–815. <https://doi.org/10.1785/0220130034>
- Stübner, K., Ratschbacher, L., Rutte, D., Stanek, K., Minaev, V., Wiesinger, R., et al. (2013). The giant Shakh dara migmatitic gneiss dome, Pamir, India-Asia collision zone, 1. Geometry and kinematics, *Tectonics*, *32*, 948–979. <https://doi.org/10.1002/tect.20057>
- Stübner, K., Grin, E., Hidy, A. J., Schaller, M., Gold, R. D., Ratschbacher, L., & Ehlers, T. (2017). Middle and Late Pleistocene glaciations in the southwestern Pamir and their effects on topography, *Earth and Planetary Science Letters*, *466*, 181–194. <https://doi.org/10.1016/j.epsl.2017.03.012>
- Teshebaeva, K., Sudhaus, H., Echtler, H., Schurr, B., & Roessner, S. (2014). Strain partitioning at the eastern Pamir-Alai revealed through SAR data analysis of the 2008 Nura earthquake, *Geophysical Journal International*, *198*(2), 760–774. <https://doi.org/10.1093/gji/ggu158>
- Thomas, J.-C., Chauvin, A., Gapais, D., Bazhenov, M. L., Perroud, H., Cobbold, P. R., & Burtman, V. S. (1994). Paleomagnetic evidence for Cenozoic block rotations in the Tadjik depression (Central Asia), *Journal of Geophysical Research*, *99*(B8), 15141–15160. <https://doi.org/10.1029/94JB00901>
- Vajedian, S., Motagh, M., Wetzell, H.-U., & Teshebaeva, K. (2017). Coupling of Sentinel-1, Sentinel-2 and ALOS-2 to assess coseismic deformation and earthquake-induced landslides following the 26 June, 2016 earthquake in Kyrgyzstan, *Geophysical Research Abstracts*, *19*, EGU2017-18464-1.
- Wang, S., Xu, C., Wen, Y., Yin, Z., Jiang, G., & Fang, L. (2017). Slip Model for the 25 November 2016 Mw6.6 Aketao Earthquake, Western China, Revealed by Sentinel-1 and ALOS-2 Observations, *Remote Sensing*, *9*, 325, <https://doi.org/10.3390/rs9040325>
- Wegmüller, U., & Werner, C. (1997). Gamma SAR processor and interferometry software. *ERS Symposium on Space at the Service of Our Environment*, Florence, Italy.
- Wegmüller, U., Werner, C., Strozzi, T., Wiesmann, A., Frey, O., & Santoro, M. (2016). Sentinel-1 Support in the GAMMA Software, *Procedia Computer Science*, *100*, 1305–1312. <https://doi.org/https://doi.org/10.1016/j.procs.2016.09.246>

- Weiss, J. R., Walters, R. J., Morishita, Y., Wright, T. J., Lazecky, M., Wang, H., et al. (2020). High-Resolution Surface Velocities and Strain for Anatolia From Sentinel-1 InSAR and GNSS Data, *Geophysical Research Letters*, *47*(17). <https://doi.org/10.1029/2020GL087376>
- Wessel, P., Smith, W. H. F., Scharroo, R., Luis, J. F., & Wobbe, F. (2013). Generic Mapping Tools: Improved version released, *EOS Transactions AGU*, *94*, 409–410. <https://doi.org/10.1002/2013EO450001>
- Wilkinson, R., Daout, S., Parsons, B., Walker, R., Pierce, J., & Ischuk, A. (2021). A Time Series InSAR Study of Faulting Around Dushanbe (Tajikistan), Fringe 2021, 11th International Workshop on “Advances in the Science and Applications of SAR Interferometry and Sentinel-1 InSAR”, 31 May–4 June 2021. Presentation available at <https://www.youtube.com/watch?v=u1-ok689wWw>
- Wright, T. J., Parsons, B. E., & Lu, Z. (2004). Toward mapping surface deformation in three dimensions using InSAR, *Geophysical Research Letters*, *31*, L01607. <https://doi.org/https://doi.org/10.1029/2003GL018827>
- Yu, C., Li, Z., Penna, N. T., & Crippa, P. (2018). Generic Atmospheric Correction Model for Interferometric Synthetic Aperture Radar Observations, *Journal of Geophysical Research: Solid Earth*, *123*(10), 9202–9222. <https://doi.org/10.1029/2017JB015305>
- Zhan, Z., & Kanamori, H. (2016). Recurring large deep earthquakes in Hindu Kush driven by a sinking slab, *Geophysical Research Letters*, *43*(14), 7433–7441. <https://doi.org/10.1002/2016GL069603>
- Zubovich, A. V., Wang, X. Q., Scherba, Y. G., Schelochkov, G. G., Reilinger, R., Reigber, C., et al. (2010). GPS velocity field of the Tien Shan and surrounding regions, *Tectonics*, *29*(TC6014), 1–23. <https://doi.org/10.1029/2010TC002772>
- Zubovich, A. V., Schöne, T., Metzger, S., Mosienko, O., Mukhamediev, S., Sharshebaev, A., & Zech, C. (2016). Tectonic interaction between the Pamir and Tien Shan observed by GPS, *Tectonics*, *35*(2), 283–292. <https://doi.org/10.1002/2015TC004055>

## Figure captions

**Figure 1.** Tectonic setting of the Greater Pamir, Global Navigation Satellite System (GNSS) velocities, and Interferometric Synthetic Aperture Radar (InSAR) data coverage. a) Major Cenozoic tectonic structures (completed from Abdulhameed et al., 2020; Käbner et al., 2016; Schurr et al., 2014) of the western edge of the India-Asia collision zone. Inset locates the study area in the India-Asia collision zone. Transparent gray arrows give bulk kinematics. Historical M6-7 earthquakes—potentially influencing our analysis—are plotted as red and purple focal mechanisms (the purple mechanism refers to a mantle earthquake; references in text and GEOFON data center). The Kharatag earthquake is poorly located. Contours give depth of the intermediate-depth earthquakes of the Hindu Kush and Pamir slabs (after Schurr et al., 2014). PFT: Pamir Frontal Thrust, MPTS: Main Pamir Thrust System, SKFS: Sarez-Karakul fault system. b) Eurasian-fixed GNSS rates (Metzger et al., 2020), major Cenozoic faults and folds (red lines), background seismicity—scaled by size from Kufner et al. (2018, 2021) as green and

from Bloch et al. (2021a) as blue circles—, and river systems. Intermediate-depth earthquakes (>200 km depth) highlight the mantle portion of the Pamir slab (pink dots) and the Hindu Kush slab (purple dots; Kufner et al., 2021). c) Interferometric database containing six frames acquired in ascending LOS (blue) and seven frames in descending LOS (red) view direction. Yellow polygon marks region where the LOS rates were decomposed into east and vertical components using interpolated north rates, shown in d), based on available GNSS rates (circles), including eight artificial (interpolated) rates to stabilize the sparsely-occupied regions (black squares).

**Figure 2.** a) East and b) vertical InSAR rates, plotted on topography and simplified fault map. c) to e) highlight areas with specific short-wavelength features discussed in the text. Salt diapirs are from Figure 11 in Gaġala et al. (2020); the salt plug and the Hoja Mumin salt fountain are active. East rates are compared to GNSS rates (vectors and color-coded circles); color scales are saturated. White arrows mark GNSS rates in the Tajik depression that were excluded as outliers. Focal mechanisms indicate crustal (dark green,  $M > 6$ ) and slab break-off (at 200 km, purple,  $M_w 7.5$ ) earthquakes that occurred during the data acquisition period (references in text). Purple and pink dots outline the intermediate-depth earthquakes (>200 km depth) of the Hindu Kush and Pamir slabs, respectively. The transparent, light blue lines in a) and b) represent the modeled rupture trace of the 2015  $M_w 7.2$  Sarez earthquake (Metzger et al., 2017). Markers “1” to “4” locate artifacts, i.e., frame-overlap jumps in the corners and edges of frames. Markers “a” to “j” locate features that we discuss in detail in the text. DF: Darvaz fault zone, IF: Ilyak fault, KTS: Kyzilart transfer zone, MF: Muji fault, OF: Officers Range, PFT: Pamir Frontal Thrust, PTS: Pamir Thrust System, SKFS: Sarez-Karakul fault system; HM: Hoja Mumin salt fountain, LK: Lake Karakul, LS: Lake Sarez, NR: Nurak reservoir.

**Figure 3.** InSAR rates in the Tajik depression, compared to background seismicity (circles and focal mechanisms; Ekström et al., 2012; Kufner et al., 2018, 2021), and plotted on detailed fault-fold map. The focal mechanisms are colored according to fault type: red, strike-slip; orange, normal; blue, thrust; turquoise, thrusts with one sub-horizontal fault plane. Thin gray lines mark extent of interferometric frames. a) East rates are compared to GNSS rates (color-coded squares and arrows). b) Vertical rates; white frames mark agricultural land use, based on MDA US BaseVue 2013 Landsat 8 data. Cross sections A to D are shown in Figures 4a and 4b. Markers “d”, “h”, and “j” locate features that we discuss in detail in the text. NR: Nurak reservoir.

**Figure 4.** Topographic profiles (max., mean, min. values within 5-km swath), InSAR horizontal and vertical rates, and background seismicity (Kufner et al., 2018) projected onto geologic cross-sections A to D through the Tajik depression (Gaġala et al., 2020; see Figure 3 for location) with the main structural features named (compare Figures 1 to 3). Markers E (east), H (location marker), I (location marker), NR (Nurak reservoir), and W (west), and envelopes A and B locate features that we discuss in detail in the text.

**Figure 5.** East rates across the Ilyak fault in a) map view and b) as across-fault profile. Background seismicity and focal mechanisms (Kufner et al., 2018) are plotted in red. The

profiles in b) are centered along the maximum rate change and are color-coded along strike, indicating different slip behavior. Median rates are plotted in purple, median topography and its deviation is indicated in green. c) Sites that characterize structural data from selected deformation zones north and south of the Ilyak fault, which is badly exposed, mostly due to its anthropogenic overprint. Pure top-to-south thrusting emplaced the crystalline basement of the Tian Shan onto Cretaceous limestone (1893A); the two sites in the Vakhsh anticlinorium characterize that part of the Tajik fold-thrust belt where the overall ~N-striking thrusts bend into the Ilyak fault zone; they have dextral-transpressive top-to-(N)NW kinematics. Structural data are plotted in lower hemisphere, equal area stereograms. Arrows around the stereograms indicate sub-horizontal maximum stress orientations determined from fault-slip analysis (following Sperner & Ratschbacher, 1994). Faults are drawn as great circles and shear directions and striae (slickenlines) as arrows pointing in the direction of the displacement of the hanging wall. Confidence levels of slip-sense determination are expressed in the arrowhead style: solid, certain; open, reliable; half, unreliable. Lithology and strata age (Cr<sub>1</sub>: Lower Cretaceous, Cr<sub>2</sub>: Upper Cretaceous, Pg<sub>3</sub>-N<sub>1</sub>: Oligocene-Miocene), and reduced stress-tensor calculations are plotted on the right (principal stress orientations:  $\sigma_1$ ,  $\sigma_2$ ,  $\sigma_3$ ;  $\theta$  fracture angle used for calculation; R is the shape factor of the stress-ellipsoid,  $(\sigma_2 - \sigma_3)/(\sigma_1 - \sigma_3)$ ; n: number of data used for calculation; dimensionless Mohr diagram visualizes normal versus shear stress relations for each fault (circles). tg: tensions gashed plotted as poles to the planes, s<sub>0</sub>: bedding. Transparent beach balls outline compressional (grey) and extensional (white) dihedra.

**Figure 6.** High-pass filtered horizontal displacement map that suppresses the regional component for the northern part of the Kafirnigan anticlinorium superposed over a shaded relief map. Kernel size is 7 pixels, i.e., ~2800 m. The east-facing scarp slopes of east-facing hogback ridges (“E” markers) show narrow but pronounced positive, the west-facing scarp slopes negative, less pronounced horizontal displacement anomalies. Sign change follows the crests of the topographic hogback ridges, suggesting divergent ground motions. These short-wavelength patterns—superimposed on the regional displacement profiles—are likely related to active gravitationally-induced mass movements. b) Structural evidence for NW-directed mass movement: along a steeply-west-dipping slope in the NW-dipping strata of the Karshi anticline (site 1795B), an Upper Cretaceous shale-gypsum sequence shows dominantly west-directed normal faulting, with the faults planes and numerous tension gashes infiltrated by gypsum. See text for discussion.

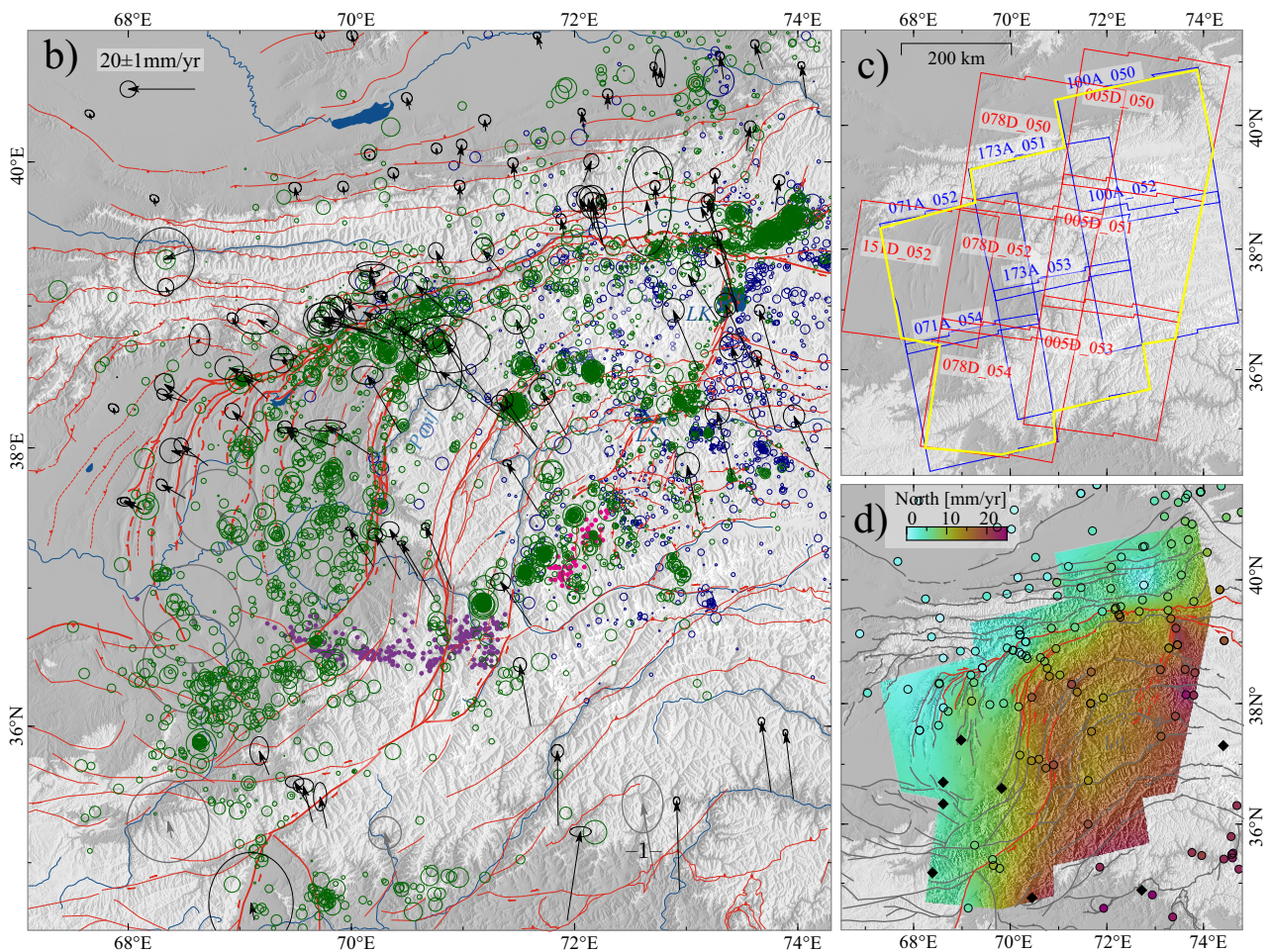
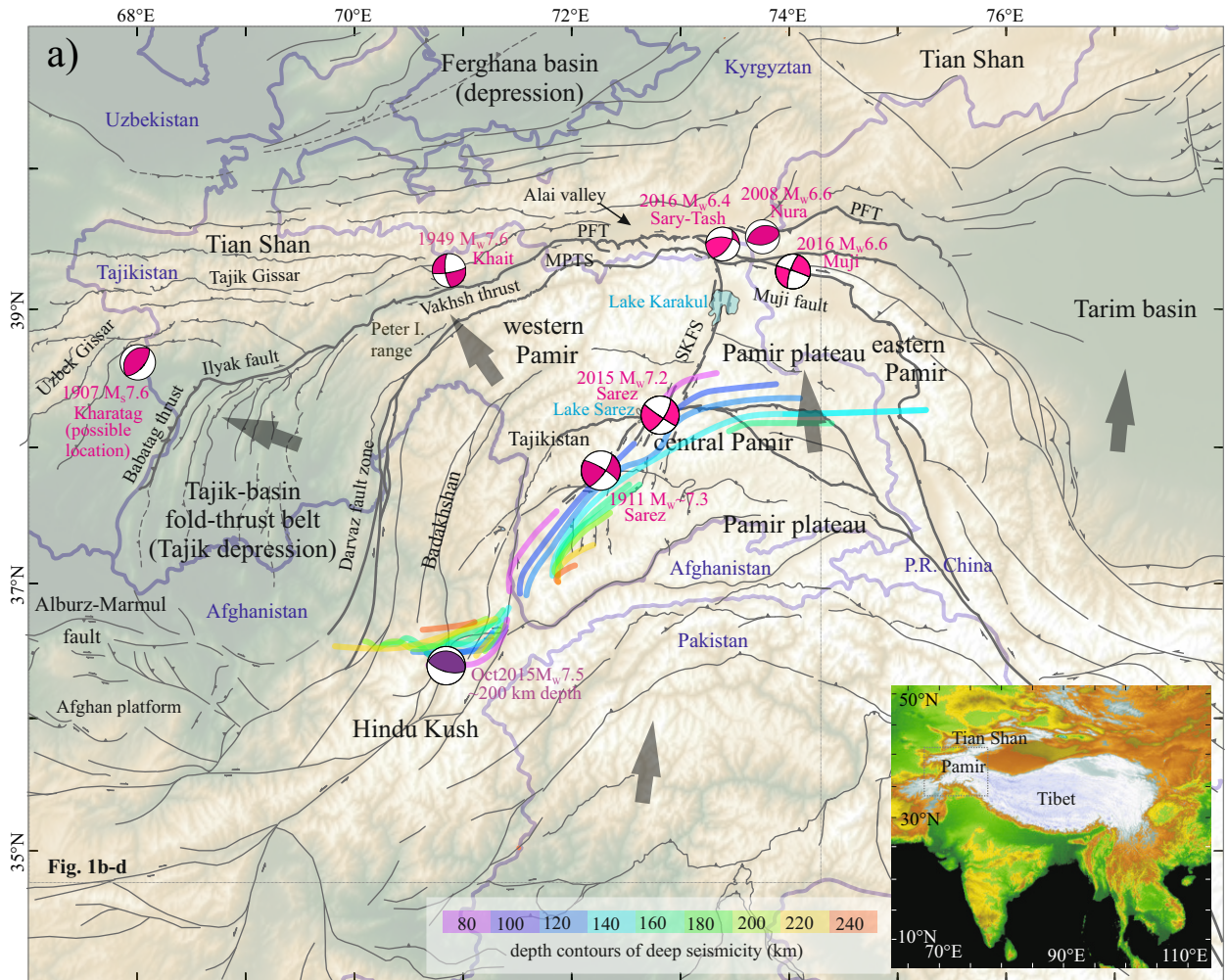


Figure 1.

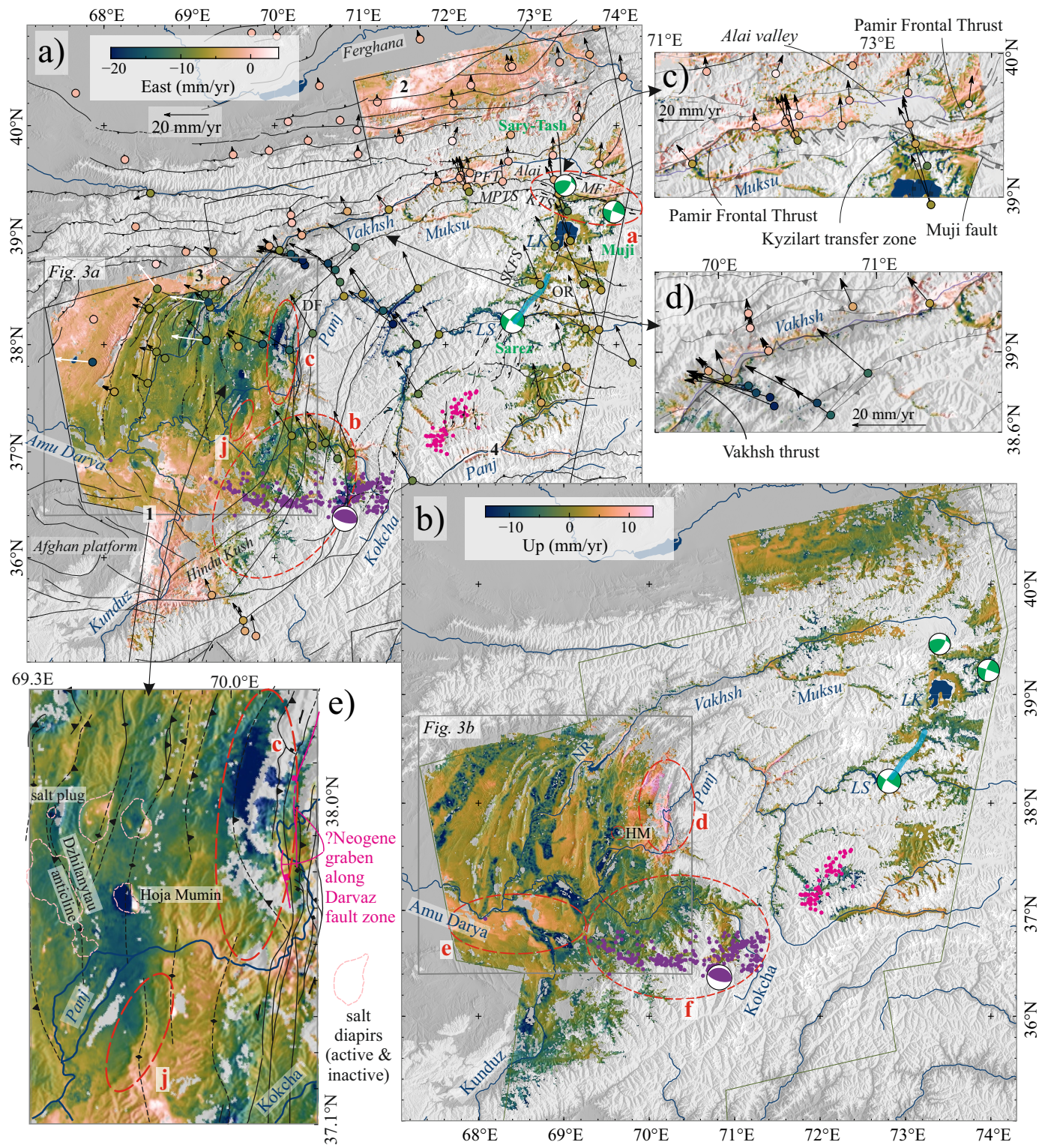


Figure 2.

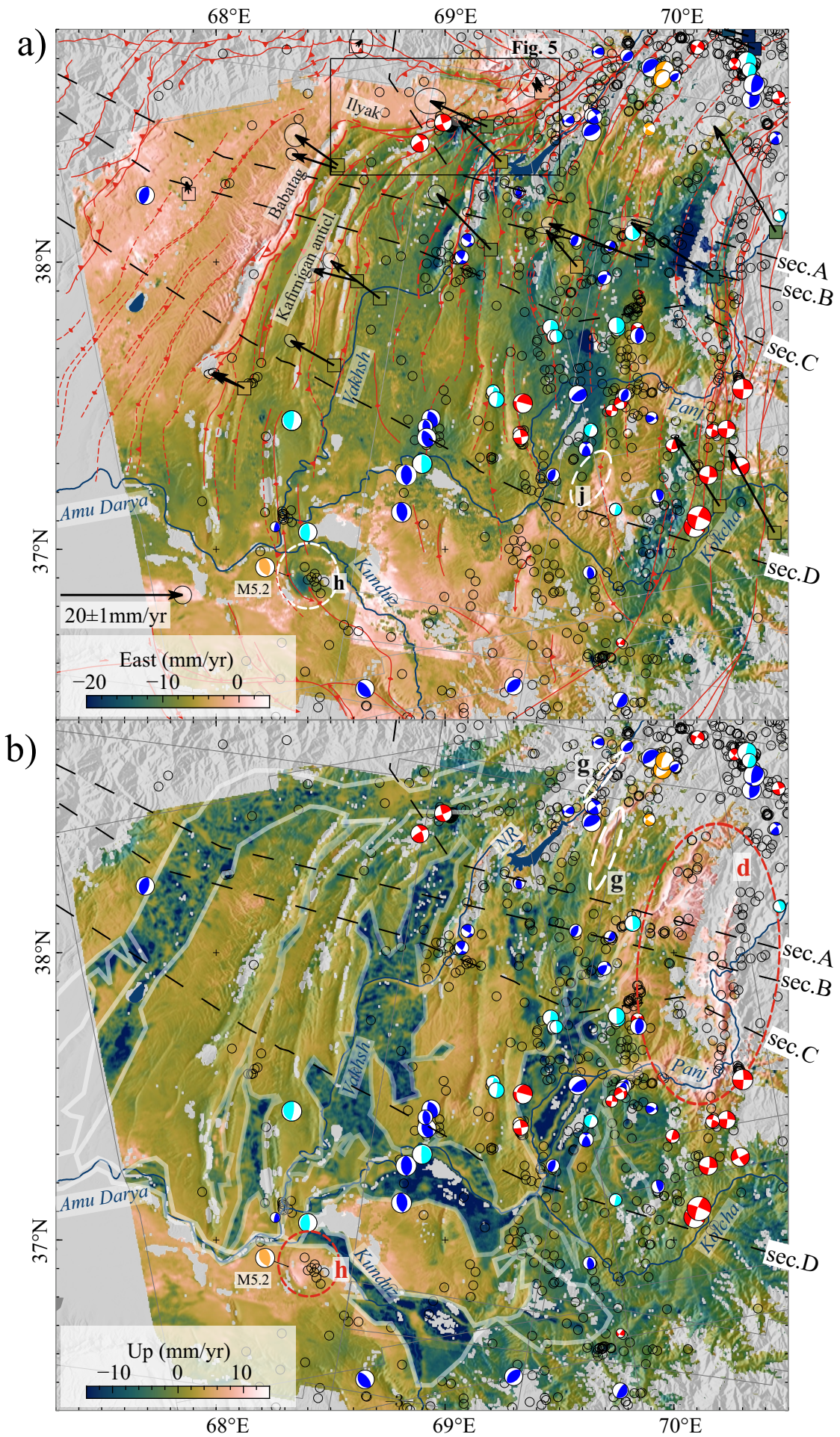


Figure 3.

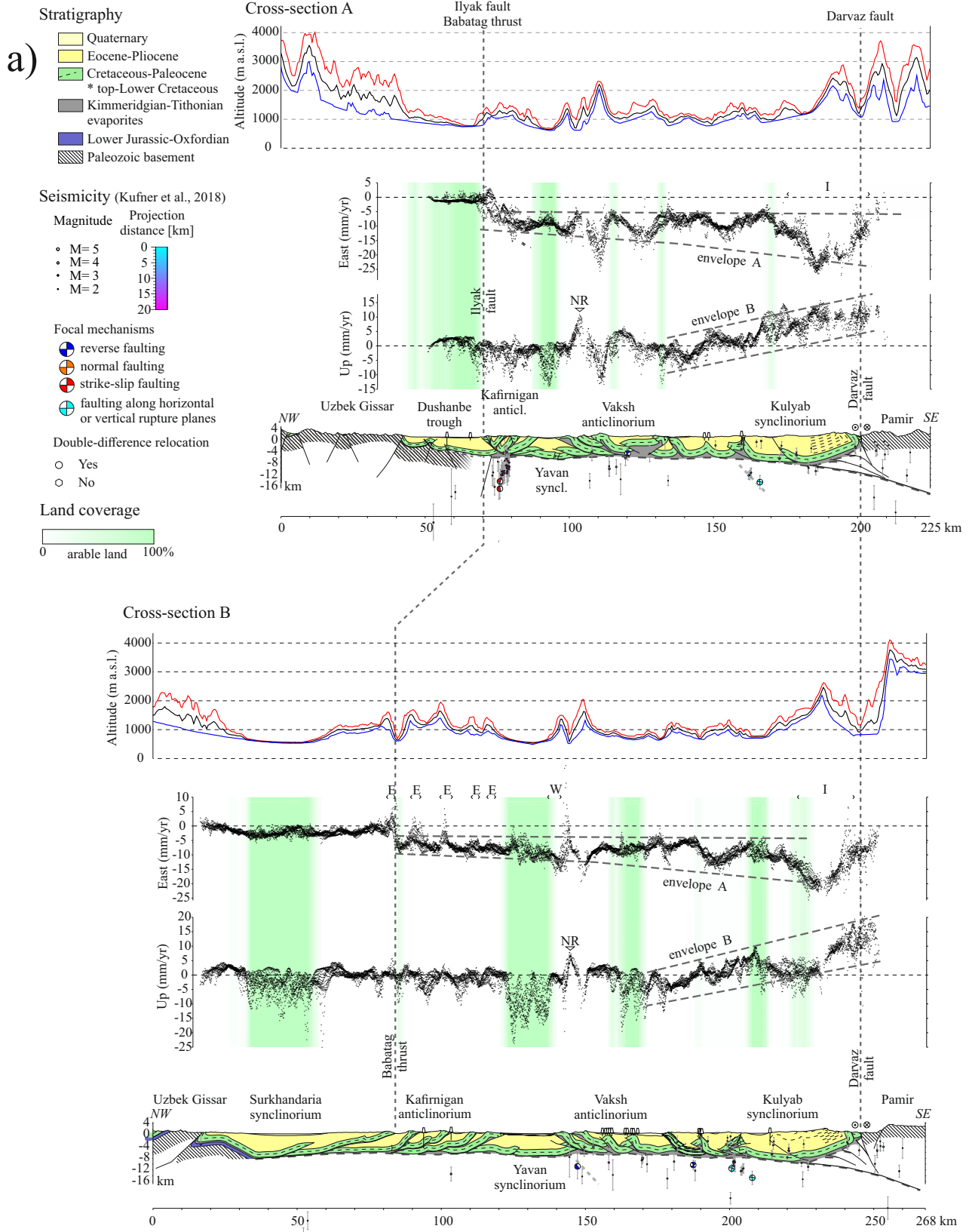
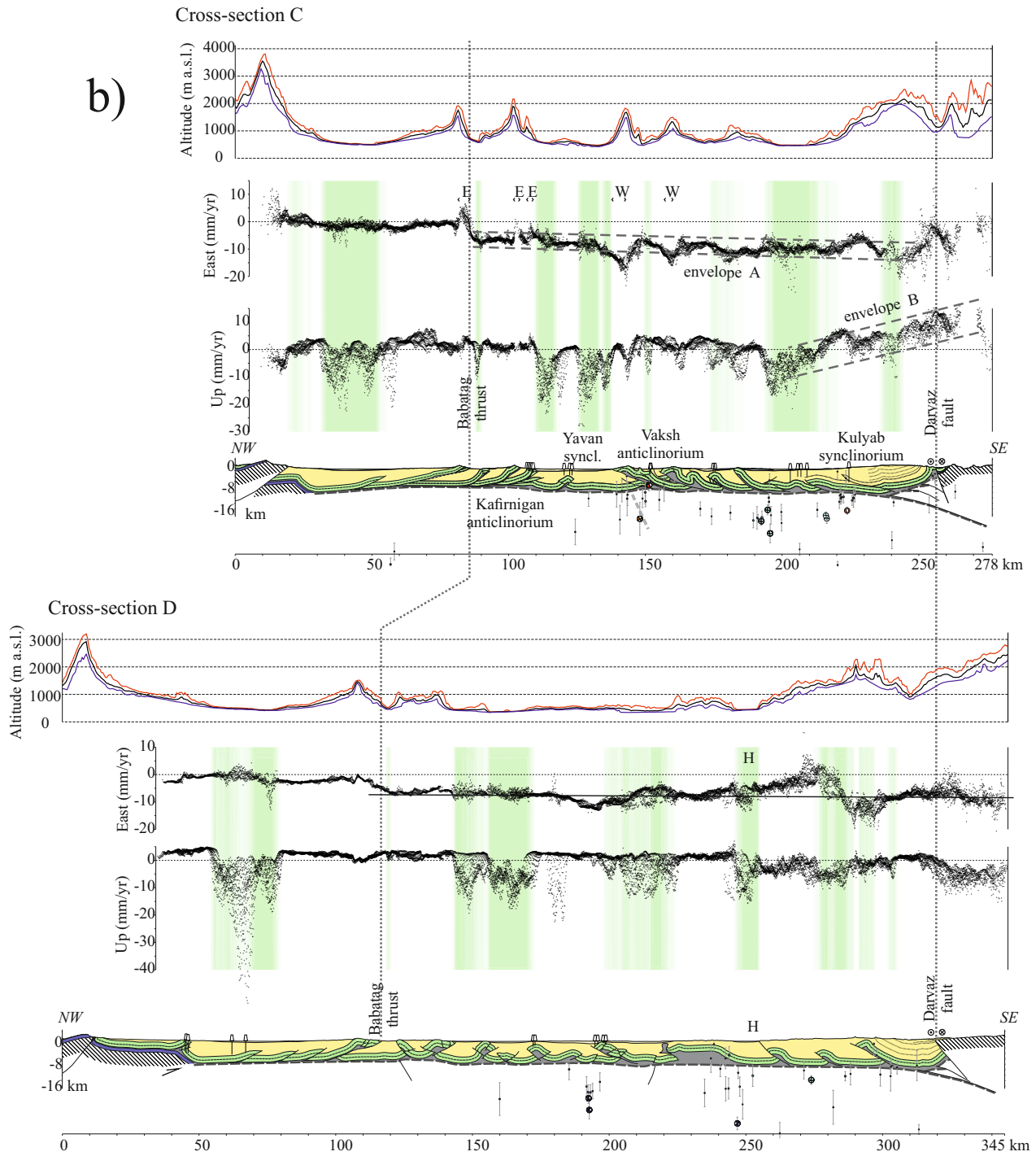


Figure 4.



**Figure 4.** (continued)

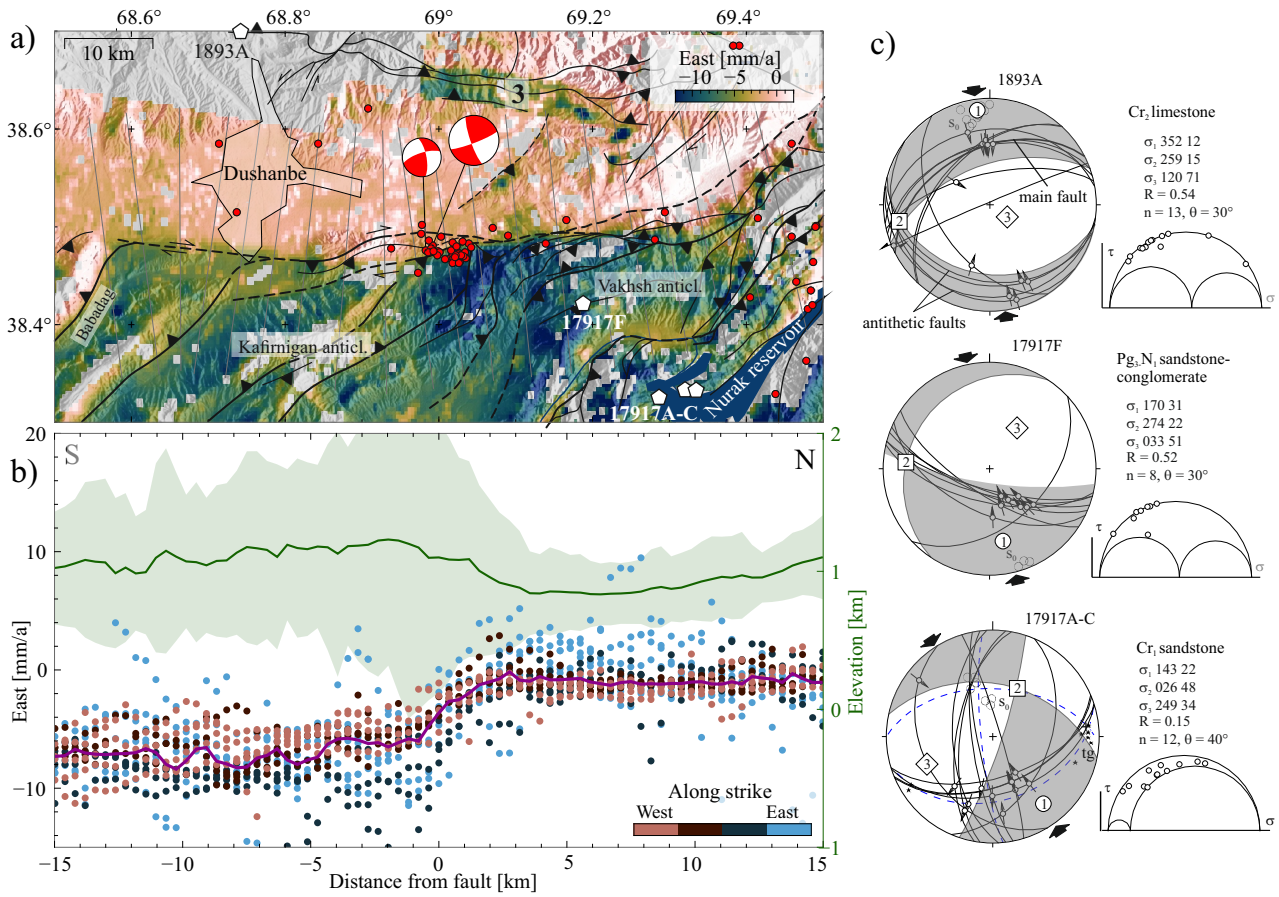


Figure 5.

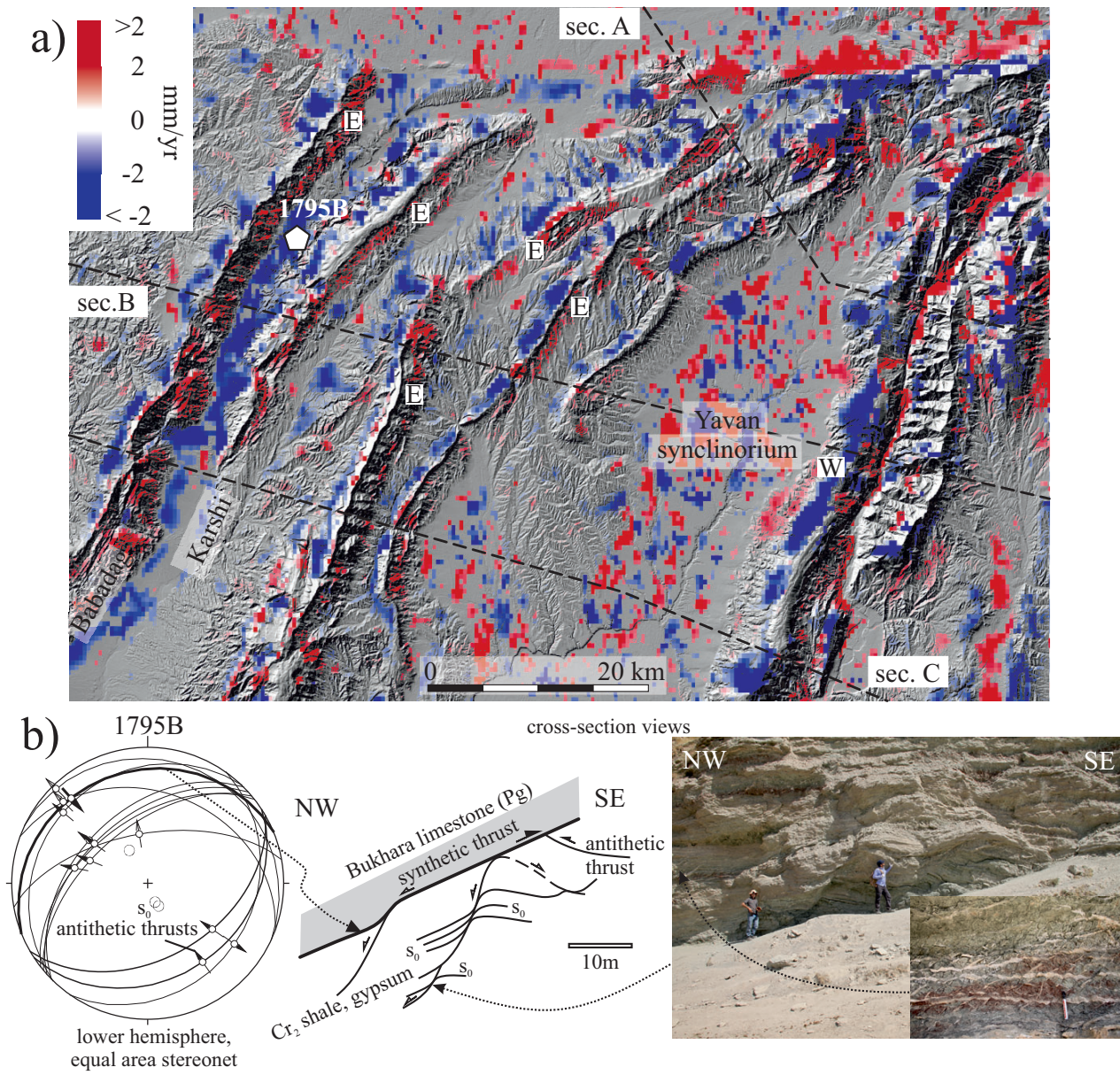


Figure 6.

# Supporting Information for "Tajik Depression and Greater Pamir Neotectonics from InSAR Rate Maps"

Sabrina Metzger<sup>1</sup>, Łukasz Gągała<sup>2,3</sup>, Lothar Ratschbacher<sup>2</sup>, Milan Lazecký<sup>4</sup>,  
Yasser Maghsoudi<sup>4</sup>, Bernd Schurr<sup>1</sup>

<sup>1</sup>Helmholtz Center, Research Center for Geosciences, Potsdam, Germany

<sup>2</sup>Geologie, Technische Universität Bergakademie Freiberg, Freiberg, Germany

<sup>3</sup>Now at Hellenic Petroleum, Marousi, Greece

<sup>4</sup>COMET, School of Earth and Environment, University of Leeds, United Kingdom

## Contents of this file

1. Supplementary text to Section 3.2 of the main text: Here, we explain how we tied the individual LOS rate maps to the GNSS reference frame and how we decomposed the LOS rates into east and up rates.

2. Tables S1 to S2.

3. Figures S1 to S12.

## Supporting material in Metzger et al. (2021b)

<https://doi.org/10.5880/GFZ.4.1.2021.005>

1. **RateMaps.zip** – InSAR rate maps and auxiliary information in geotiff-format: linear rates, uncertainties, and LOS information of individual frames (labeled by frame number); concatenated and decomposed east and up rates and interpolated GNSS north rates (all in the stable Eurasian reference frame ITRF2014, Altamimi et al., 2017) and corresponding uncertainties.

---

Corresponding author: Sabrina Metzger, metzger@gfz-potsdam.de

## 1. From LOS rates to East/Vertical rates in a GNSS-fixed reference frame

We corrected each rate map with a linear ramp to optimize the fit to the horizontal GNSS rates and the frame overlap along-track. These two conditions can be formulated as a  $M \times N$  design matrix  $G$ , which, if multiplied with  $N$  ramp parameters  $m = [m_1, \dots, m_N]^T$ , match  $M$  observations  $d = [d_1, \dots, d_M]^T$ . Uncertainties are included as data weights  $W$  resulting in  $Wd = WGm$ . If this problem is linear and over-determined, it can be solved for the best-fitting ramp parameters,

$$m = (G^T W G)^{-1} G^T W d.$$

Both conditions are met for any given three successive InSAR frames  $I1$ ,  $I2$ , and  $I3$  and the co-located GNSS rates  $G1$ ,  $G2$ , and  $G3$  (collapsed into line-of-sight) with

$$\begin{bmatrix} I1 - I2 \\ I2 - I3 \\ I1 - G1 \\ I2 - G2 \\ I3 - G3 \end{bmatrix} = \begin{bmatrix} x & y & 1 & -x & -y & -1 & 0 & 0 & 0 \\ 0 & 0 & 0 & x & y & 1 & -x & -y & -1 \\ x & y & 1 & 0 & 0 & 0 & 0 & 0 & 0 \\ 0 & 0 & 0 & x & y & 1 & 0 & 0 & 0 \\ 0 & 0 & 0 & 0 & 0 & 0 & x & y & 1 \end{bmatrix} \cdot \begin{bmatrix} a_1 \\ b_1 \\ c_1 \\ \dots \\ a_3 \\ b_3 \\ c_3 \end{bmatrix}$$

where  $x, y$  being the column and row index numbers of the merged pixel index frame and  $a, b, c$  the linear ramp parameters to be inverted for. Following Ou (2020), we weighted the InSAR rates overlapping along-track with the inverted sum of the standard deviation of the detrended overlap area, for example  $(\sigma(I1) + \sigma(I2))^{-1}$ . For the lower part of the equation, where InSAR rates are fitted to GNSS rates within a search radius of 4 km, we apply the combined weights

$$\sqrt{\frac{p}{q}} (\sigma(I1) + \sigma(G1))^{-1},$$

where the InSAR uncertainties are given by the standard deviation of all pixels within the search radius of the GNSS data point, the GNSS uncertainties are collapsed into line-of-sight (LOS) and the whole term is scaled by the square-root of the ratio of number of included InSAR data points  $p$  and GNSS data points  $q$ .

In a second step, we decomposed ascending and descending LOS rates of each rate map sample – if available – into East and Vertical rates following Ou (2020). The line-of-sight velocity  $V_{LOS}$  is defined by the heading angle  $\phi$ , measured positive clockwise from north, and the incidence angle  $\theta$ , measured from the vertical down direction,

$$V_{LOS} = -V_E \cos(\phi) \sin(\theta) + V_N \sin(\phi) \sin(\theta) + V_U \cos(\theta), \quad (1)$$

where each term defines the contribution of the east, north, and vertical component, respectively (see geometric sketch in Figure S8). Given the near-polar orbits and relatively steep look angle, this means that the individual contributions of each direction are about 40, 10 and 50 %, hence, InSAR data are least sensitive to NS-motion (see the E, N, and U contributions to the LOS unit vector in Figure S7).

As graphically shown in Figure S8, Equation (1) can be rearranged to a linear problem by making use of the Pythagorean trigonometric identity, that is  $V_{LOS}^2 = V_E^2 + V_{UN}^2$ , and the unit vector length, that is  $\vec{V}_{LOS} = \vec{V}_E + \vec{V}_{UN} = 1$ ,

$$V_{LOS} = \left[ -\cos(\phi) \sin(\theta) \quad \sqrt{1 - \cos^2(\phi) \sin^2(\theta)} \right] \cdot \begin{bmatrix} V_E \\ V_{UN} \end{bmatrix},$$

which can be inverted to obtain east ( $E$ ) and a sub-vertical ( $UN$ ) direction. Each InSAR rate pixel is weighted by its standard deviation. The associated uncertainties  $\sigma(V_E)$  and  $\sigma(V_{UN})$  are calculated by the design matrix  $G$  and the squared uncertainty matrix  $\Sigma$  via  $cov(p) = [G^T cov(d)^{-1} G]^{-1}$ , where the diagonal terms of  $cov(p)$  are the variances, respectively squared uncertainties, of  $V_E$  and  $V_{UN}$ .

The incidence angle variation across track (30-46 degrees) causes systematic errors in the rates, which are small compared to our rate uncertainties (pers. comm. Xi Ou). However, for future work, including longer time-series, this bias might become relevant.

Finally, we can extract the vertical component  $V_U$  from  $V_{UN}$  by GNSS North rate constraints. The tectonically dominant northward motion of the region is most difficult to resolve with InSAR but is well constrained by GNSS data. Thus, we fixed the north component using interpolated GNSS data (Figure 1d) and solved for  $V_U$ . We fitted a surface to the GNSS measurements and also the corresponding uncertainties using natural neighbor interpolation and subtracted it from  $V_{UN}$ ,

$$V_U = \frac{V_{UN} \cdot \sqrt{1 - \sin^2(\theta) \cos^2(\phi)}}{\cos(\theta)} - V_N \frac{\sin(\phi) \sin(\theta)}{\cos(\theta)}$$

The corresponding uncertainties were calculated by replacing the rates with the uncertainties in the above formula.

More details on the reference frame and rate decomposition can be found in Ou (2020).

**Table S1.** Interferometric data base used for SBAS inversion, after quality control, with track and frame numbers, start and end dates (in YYYYMMDD).  $\Delta T$  is the time period covered by our InSAR networks in years, and #sc and #ifgs are the number of scenes resp. interferograms used in the inversion. “Mask” denotes the percentage of masked pixels per frame. The inversion was an unweighted NSBAS least-square inversion with a gamma value of 0.0001. The coordinates indicate the rate reference point.

Track	Frame	Start date	End date	$\Delta T$ [yr]	#sc	#ifg	mask [%]	Lat.[°]	Lon.[°]
005D	050	20170312	20200507	2.98	76	196	32	73.1922	40.0142
005D	051	20180506	20200706	2.00	46	146	52	72.6672	38.3310
005D	053	20170628	20200706	2.94	54	94	46	71.4376	36.1750
071A	052	20150806	20200312	5.02	94	313	11	69.0243	36.9975
071A	054	20141010	20200312	6.00	112	354	42	69.8484	35.6594
078D	050	20171230	20200804	2.93	74	234	46	70.3022	39.8281
078D	052	20170317	20191126	2.02	64	160	45	70.2885	37.1488
078D	054	20170703	20200430	3.07	64	142	50	70.2197	36.3637
100A	050	20160814	20200618	4.01	97	335	44	72.7361	39.2707
100A	052	20170505	20200618	3.03	52	111	56	73.5527	37.5625
151D	052	20171211	20200517	3.01	70	268	9	68.2496	37.7773
173A	051	20160714	20200717	4.01	67	144	68	71.0955	38.7018
173A	053	20151129	20200518	4.97	61	126	58	71.1958	36.8771

**Table S2.** Individual LiCSBAS processing and filtering parameters sorted by frame and track number. Default masking thresholds were: average coherence of 0.05, standard rate deviation of 100 mm/yr , 10 allowed data gaps, spatio-temporal consistency of 5 mm; all other thresholds are stated below.  $T_{max}$  – required max. time length of connected (sub-)network, #i-no-loop – max. number of allowed interferograms with no loop, #loop-err – max. number of allowed interferometric triplets with significant loop errors, rms – max. allowed rms residuals after rate estimate, filt – spatial and temporal filter width. To estimate and suppress the linear height-dependence all pixels above 200 m a.s.l. were included. Each pixel has a spatial extent of 444 m along flight-track and 340–360 m across flight-track.

Track	Frame	$T_{max}$ [a]	#i-no-loop	#loop-err	rms [mm/yr]	filt [km]	filt [d]
005D	050	1.0	50	5	2	2	46
005D	051	1.0	50	<b>7</b>	<b>3</b>	2	52
005D	053	<b>0.0</b>	50	5	2	2	62
071A	052	1.0	50	5	2	2	54
071A	054	1.0	<b>15</b>	5	2	<b>5</b>	53
078D	050	<b>0.9</b>	50	5	2	2	38
078D	052	1.0	50	5	2	2	46
078D	054	1.0	50	5	2	2	49
100A	050	1.0	<b>10</b>	5	2	2	43
100A	052	<b>2.0</b>	50	5	2	2	67
151D	052	1.0	50	5	2	2	38
173A	051	1.0	50	<b>0</b>	2	2	66
173A	053	1.0	50	5	2	2	81

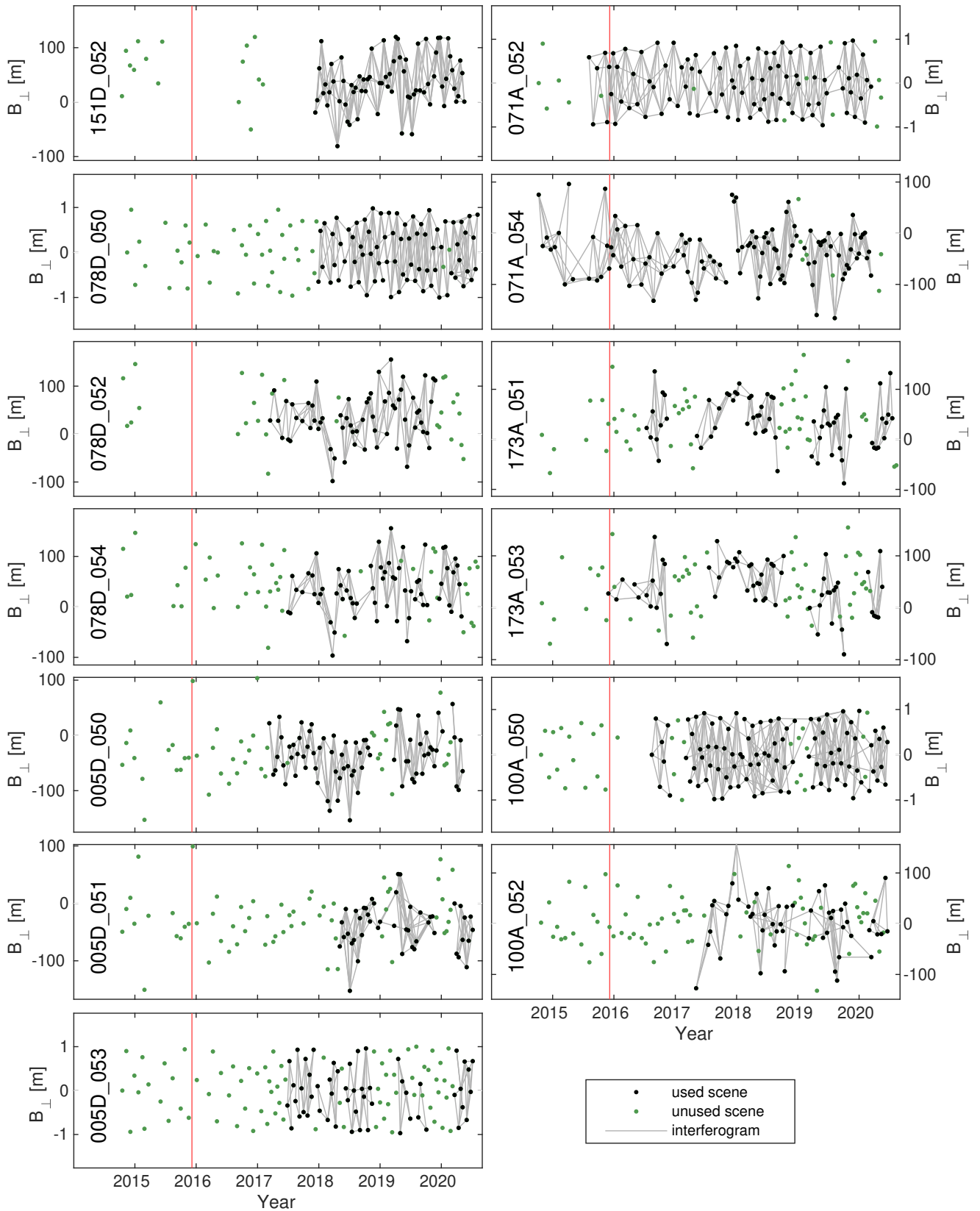


**Figure S1.** Temporal baselines and interferometric networks sorted by frame number (see Figure 1c for frame locations). Gray lines mark interferograms used in the LiCSBAS time-series analysis, green dots mark unused SAR scenes, red line marks the time of the  $M_w 7.2$  Sarez earthquake. If no information were available, the orbital baselines are randomized and normalized between  $\pm 1$ .

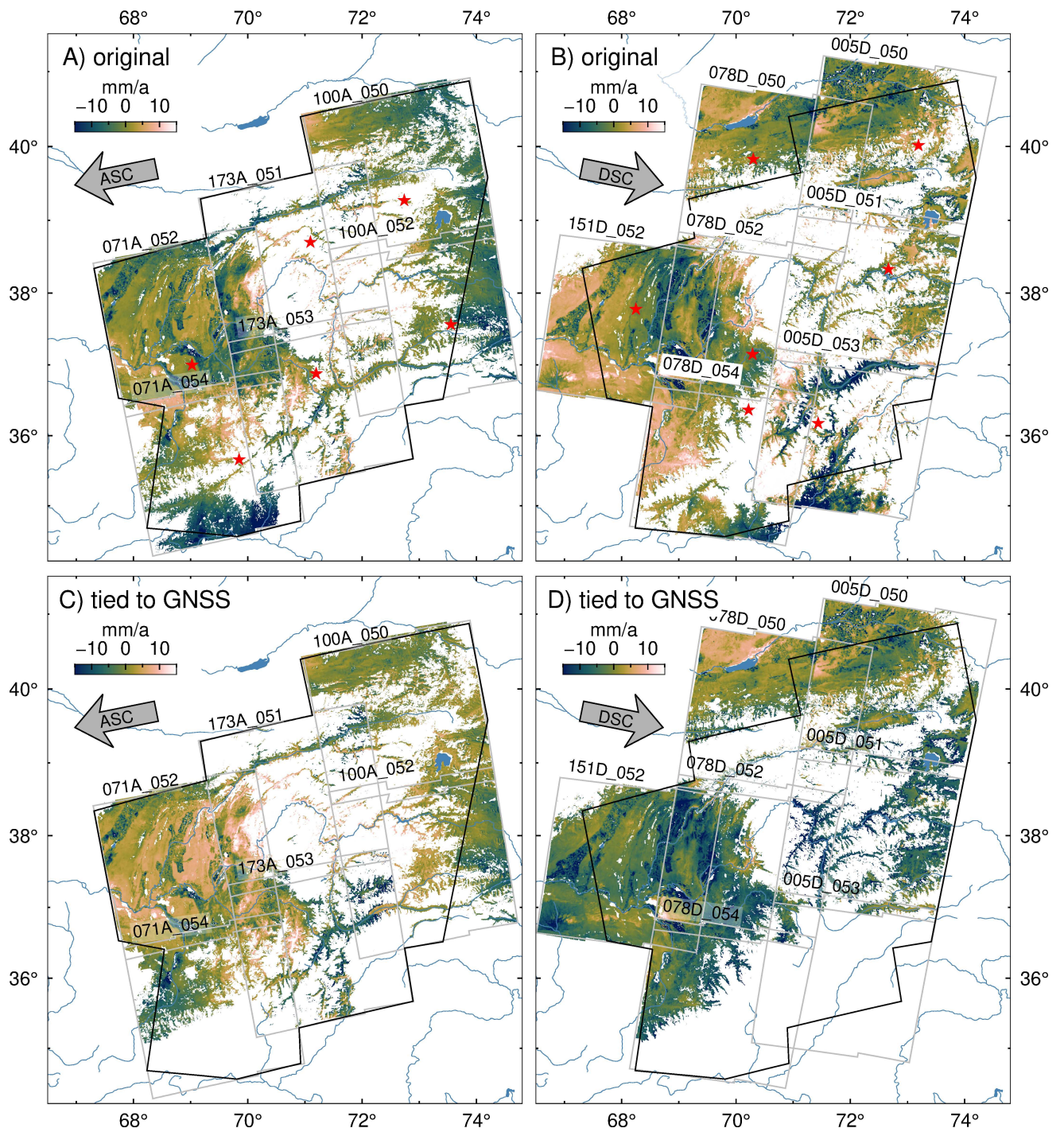


**Figure S2.** Rate maps resulting from LiCSBAS time-series analysis of A) ascending and B) descending radar frames, relative to the most stable reference point within each frame (red stars) and C) and D) after tying the rates to a Eurasia-fixed GNSS reference frame. Color scales are saturated.

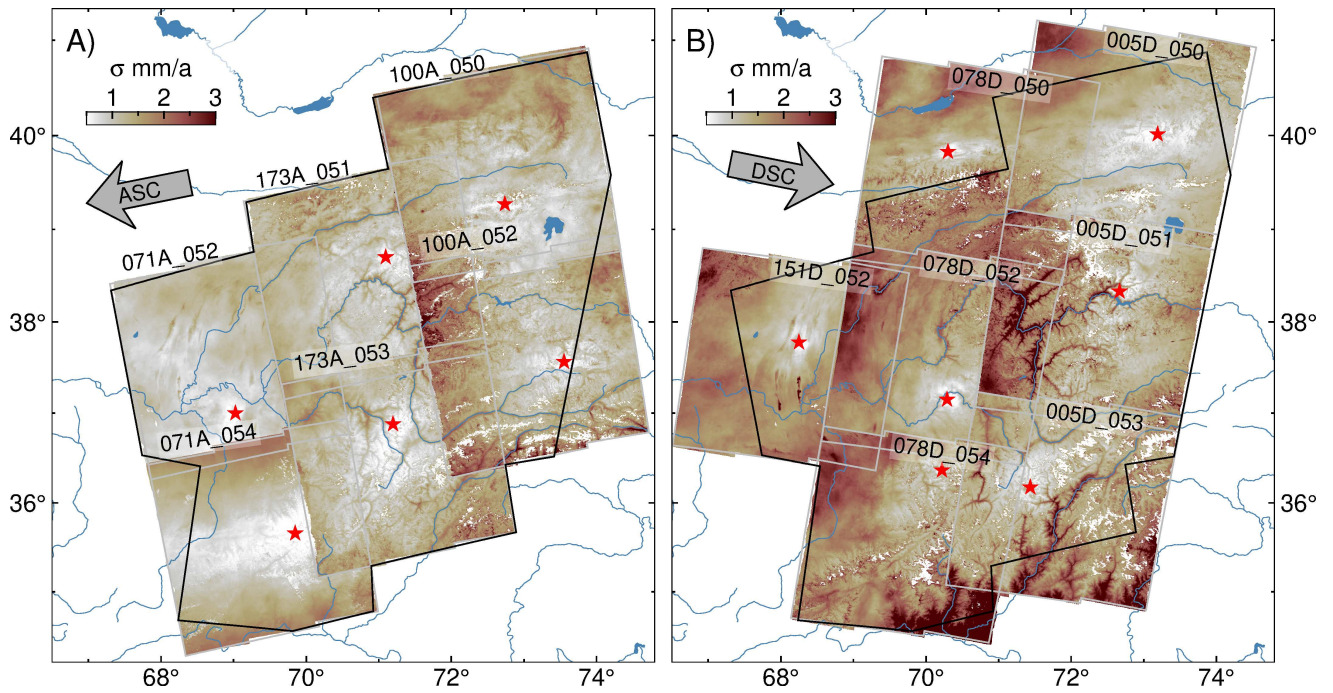


**Figure S3.** Standard deviations resulting from LiCSBAS time-series analysis of A) ascending and B) descending rate maps. Uncertainty scales with distance to the reference point. Large uncertainties are mostly caused by poorly unwrapped interferograms and/or strongly varying tropospheric conditions.

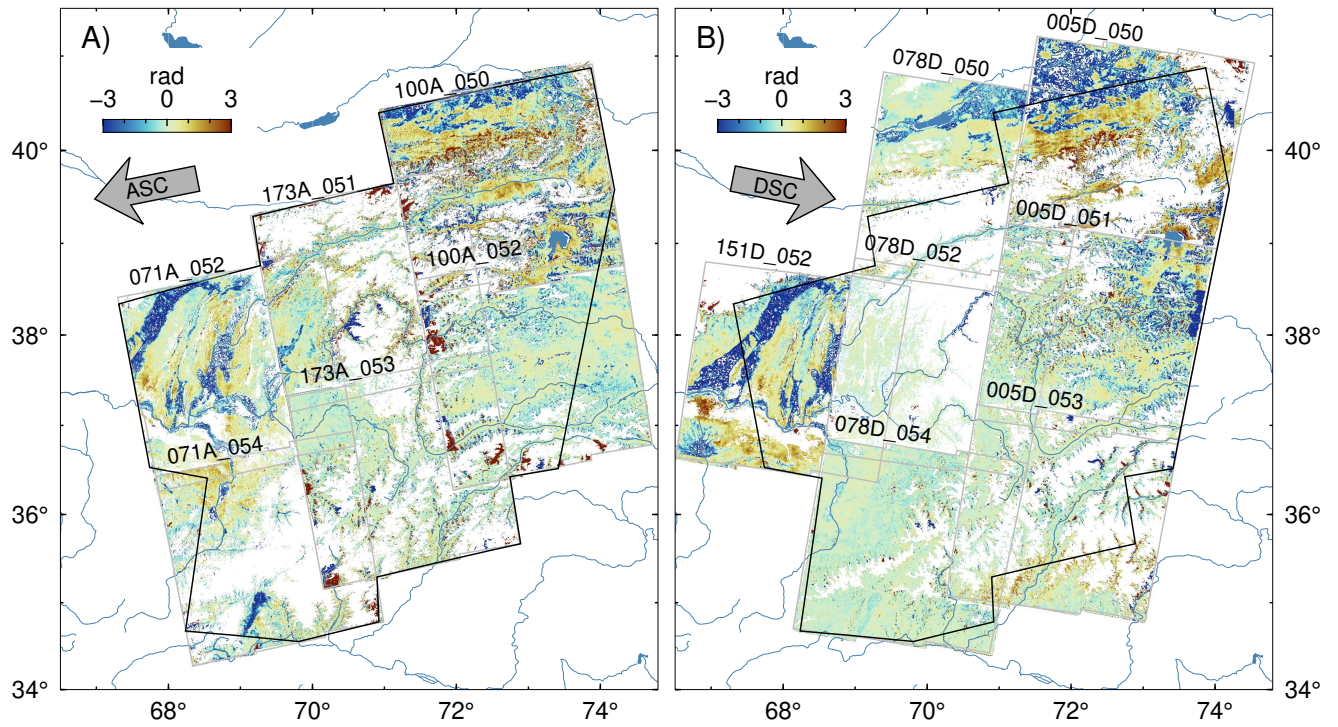


**Figure S4.** Systematic rate bias in A) ascending and B) descending frames, that is the average of 70–80 interferometric phase closure loops ( $\phi_{13} - \phi_{12} - \phi_{23}$ ) of the 2017–2020 interferograms.

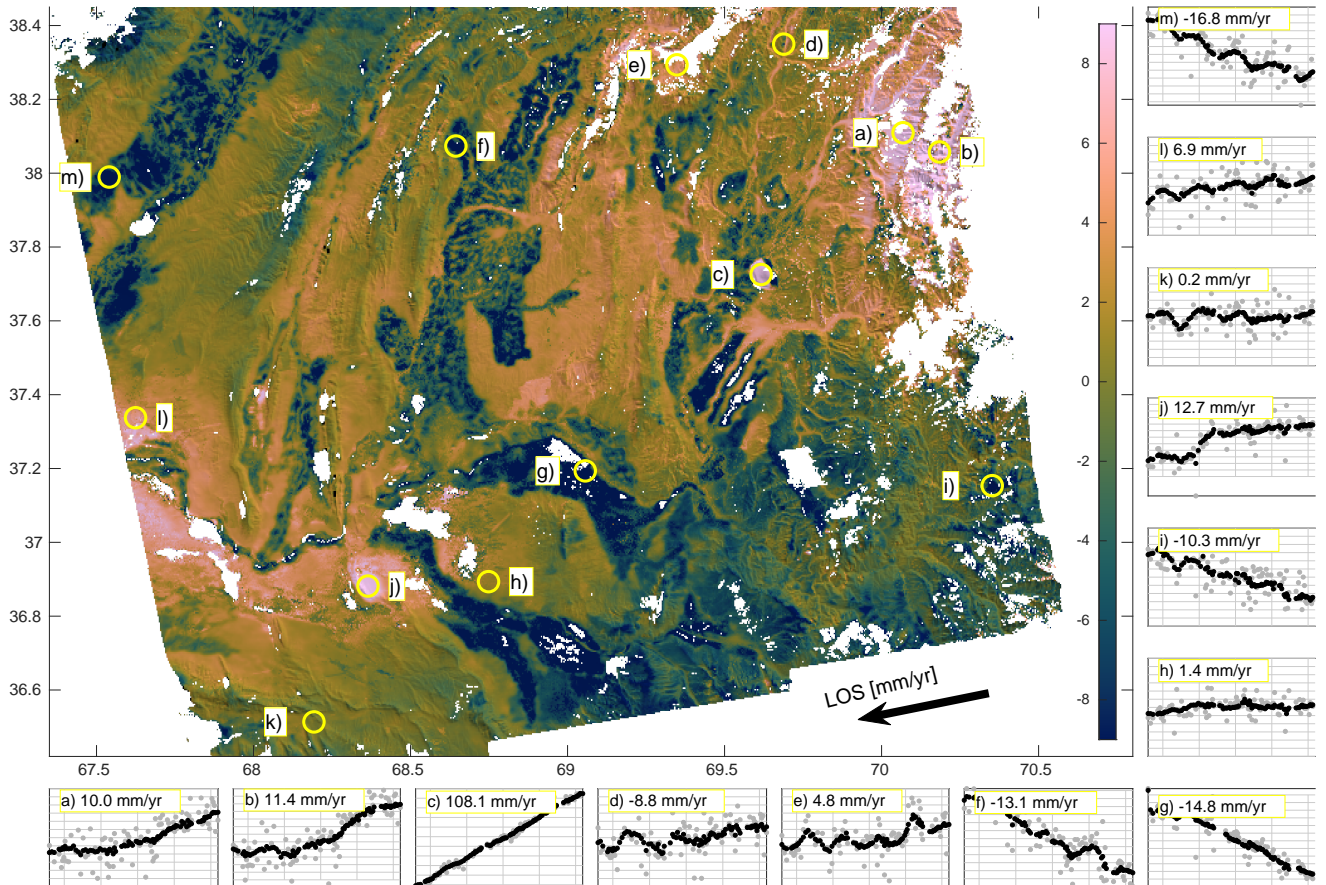


**Figure S5.** LiCSBAS line-of-sight (LOS) rate map of frame 071A\_052 and filtered (black) and unfiltered (grey) time-series of locations a) to m) (yellow circles). The horizontal and vertical bars in the subfigures mark the years 2016–2020, respectively 10 mm LOS displacement. a) and b) show non-linear behavior, probably related to the post-seismic effects following the 2015  $M_W$ 7.2 Sarez earthquake. c) is located on top of the Hoja Mumin diapir and horizontal bars mark 50 mm LOS displacement. d)-f) and i)-m) exhibit significant seasonal signal, and j) combined uplift and westward motion following a  $M_W$ 5.2 earthquake on January 9, 2017, located at marker "h" in Figure 3 of the main text.

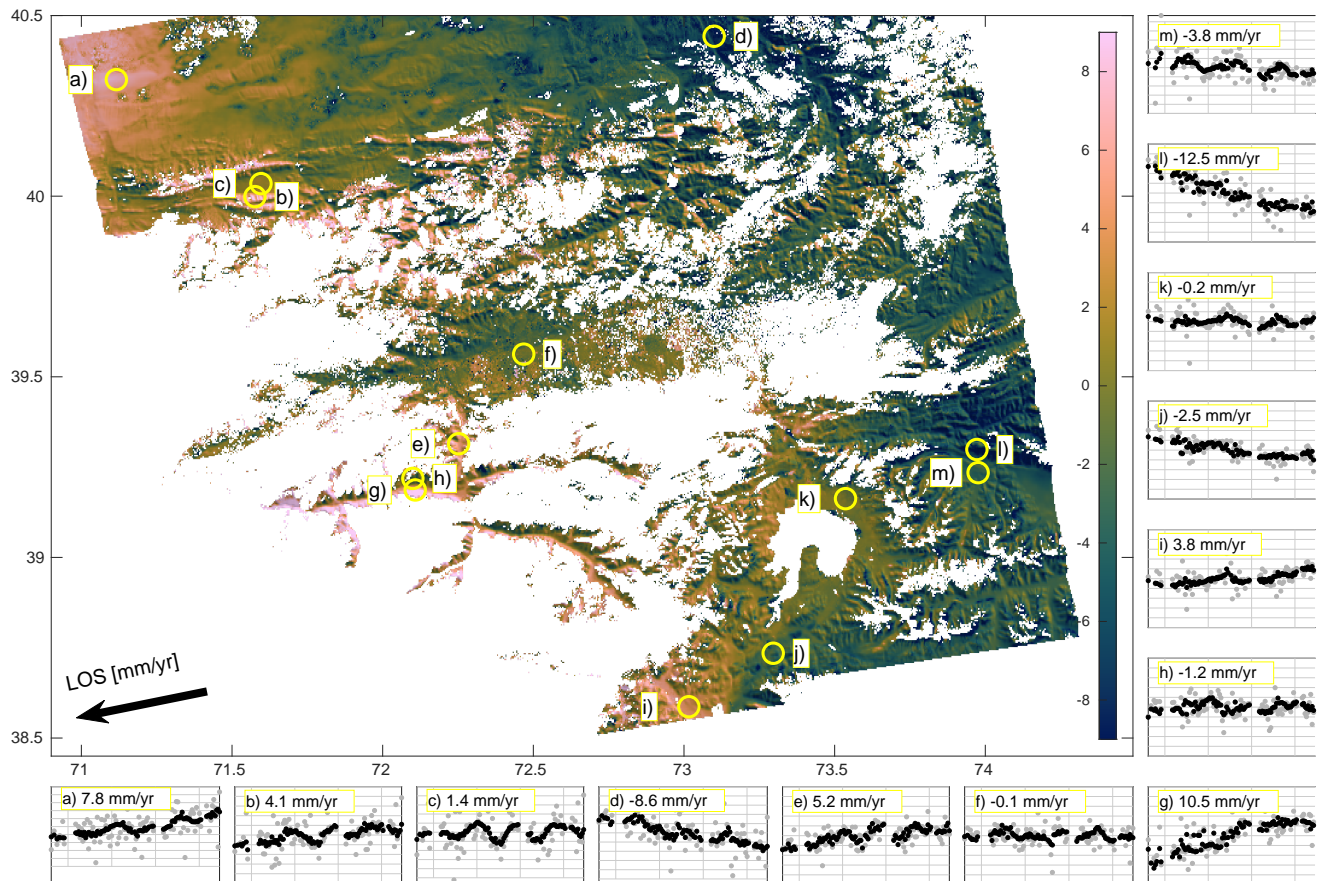


**Figure S6.** Same as Figure S5, but for frame 100A\_050. Vertical bars mark the years 2017–2020. e), g), h), i), and j) might contain non-linear components related to post-seismic effects following the 2015  $M_w$  7.2 Sarez earthquake.

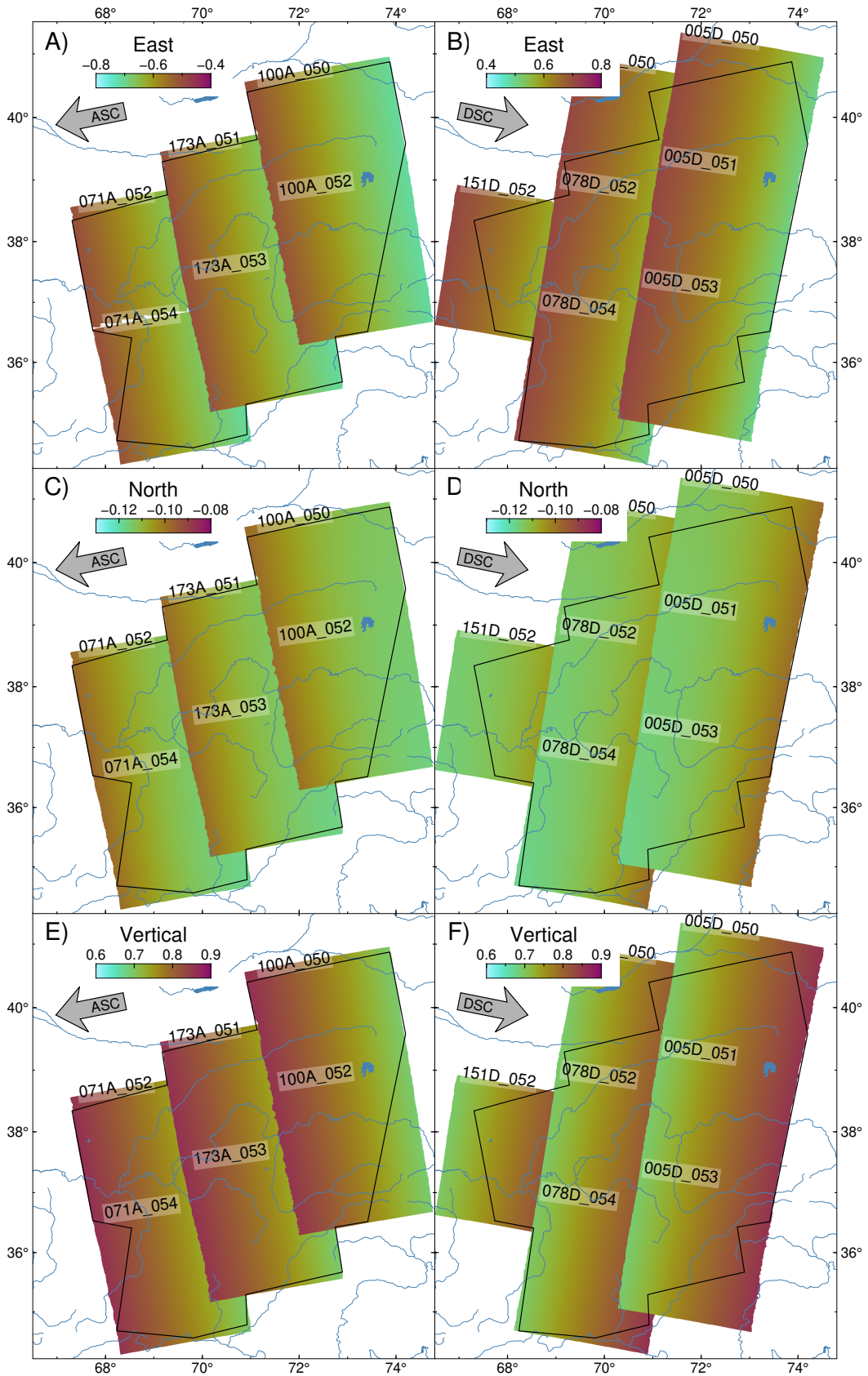


**Figure S7.** Unit values of the ascending (ASC, from left to right, track 71, 173 and 100) and descending (DSC, track 151, 078 and 005) line-of-sight vector for A), B) east, C), D) north, and E), F) vertical direction. Note the different color scales.

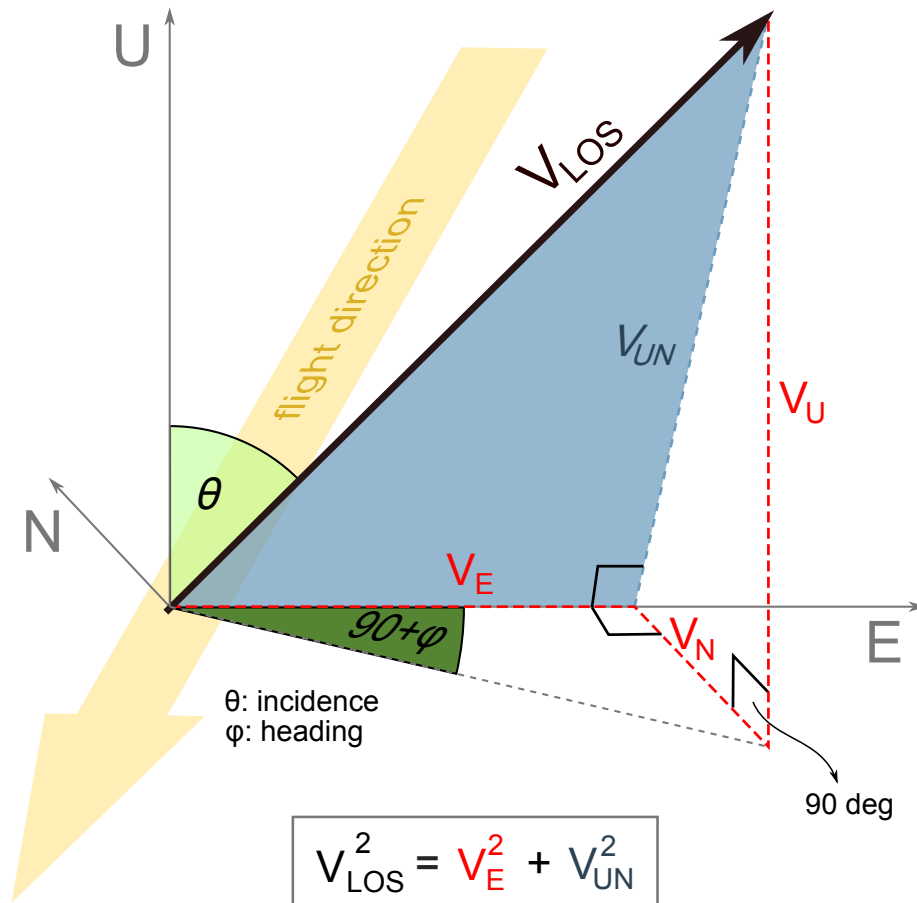


**Figure S8.** Sketch illustrating the line-of-sight acquisition geometry and Pythagorean trigonometric identity used to decompose the LOS unit vector  $V_{\text{LOS}}$  into  $V_E$  and  $V_{\text{UN}}$ , with E, N, U being east, north, up.

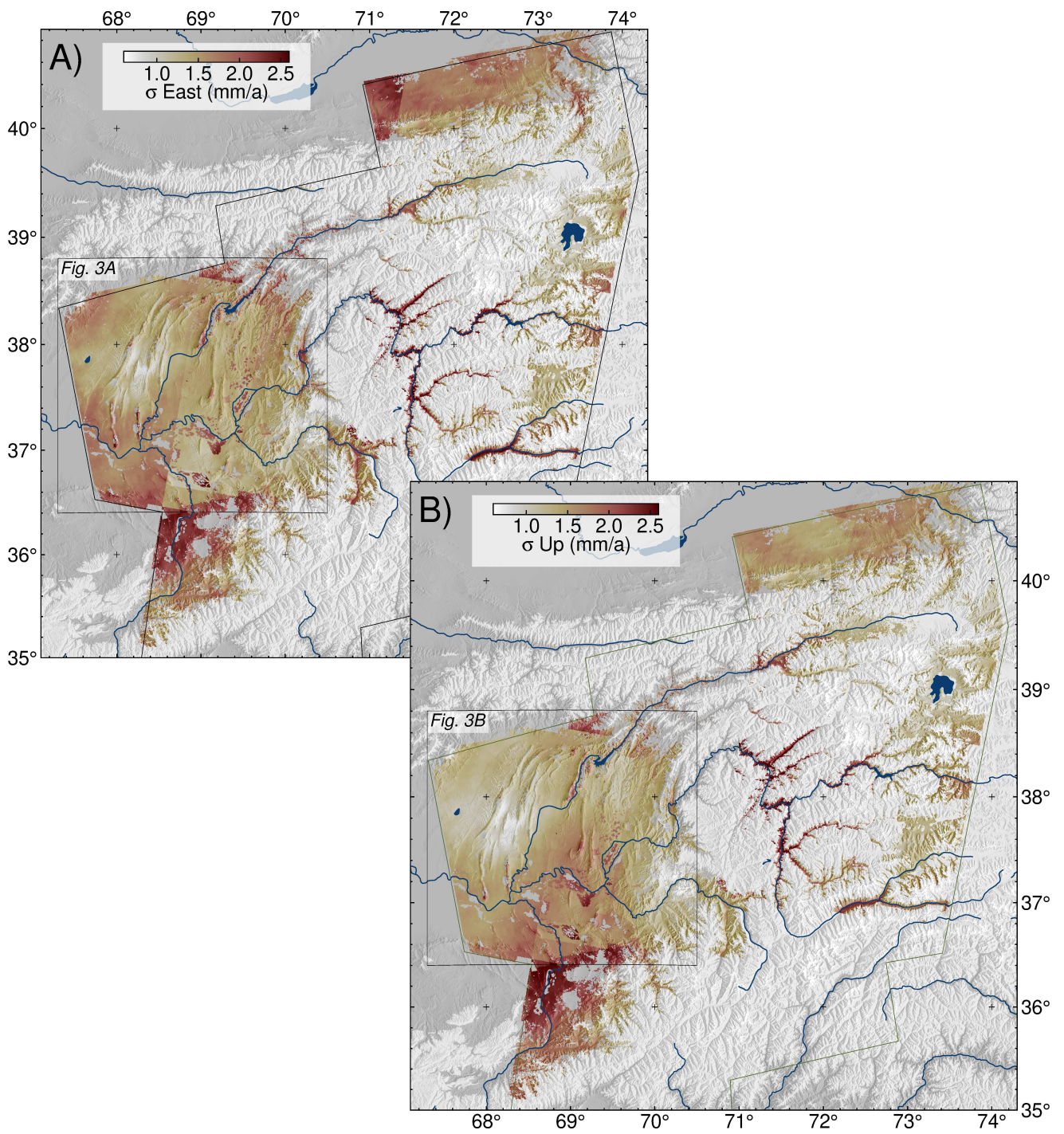


**Figure S9.** Rate standard deviation of A) east and B) vertical rates after decomposition and inclusion of GNSS rate errors.

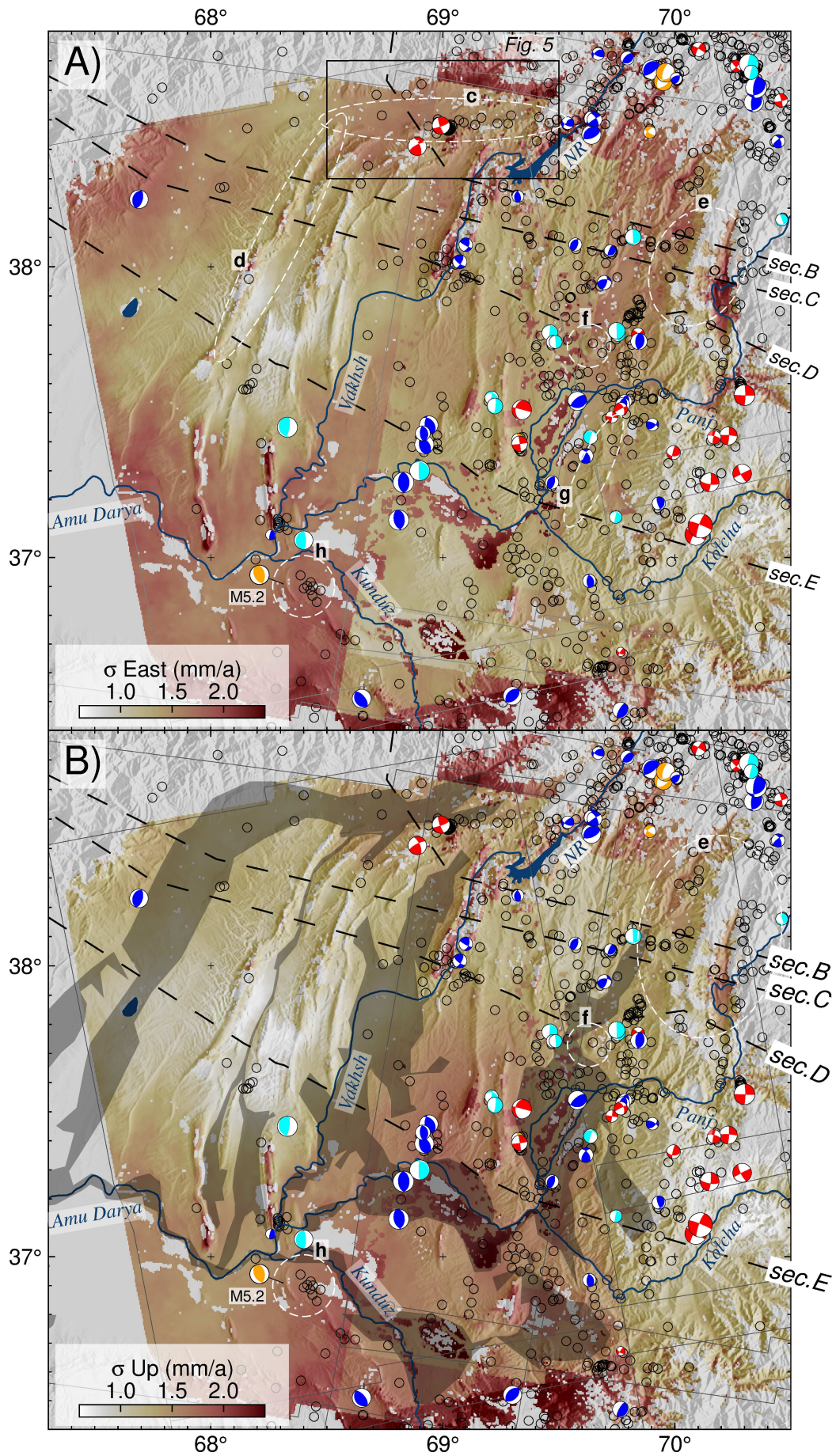


**Figure S10.** Detail view of Figure S9. See Figure 3 in the main text for other features.

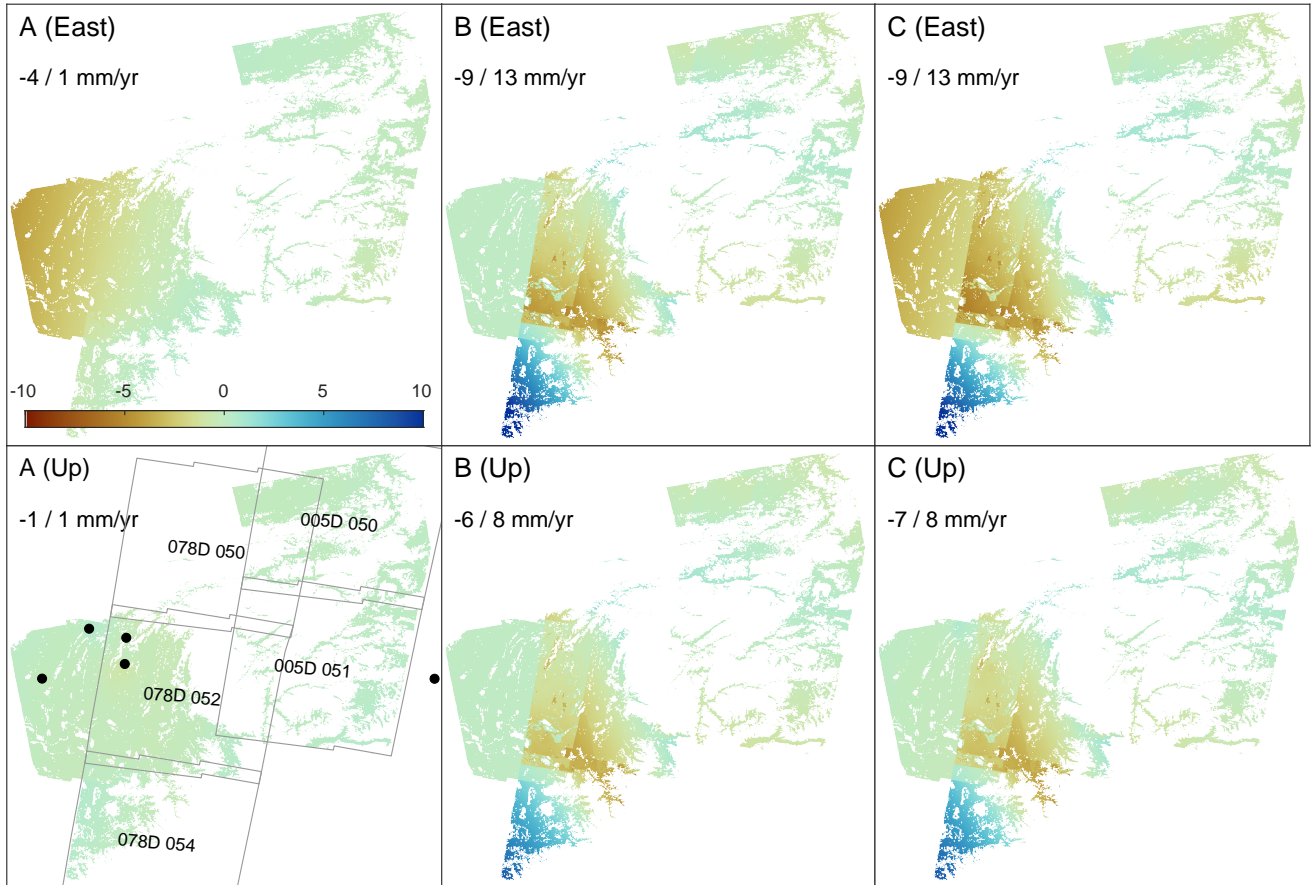


**Figure S11.** Reference frame sensitivity tests. East (top) and up (bottom) rate differences compared to our preferred solution presented in the main text, if A) the five poorly-fitting GNSS rates were included (black circles and white arrows in Figure 2 of the main text), B) the along-track overlap fits of frames 078 and 005 were optimized, and C), a combination of A) and B). Color scales are comparable, indicated numbers state min/max values of the rate differences.

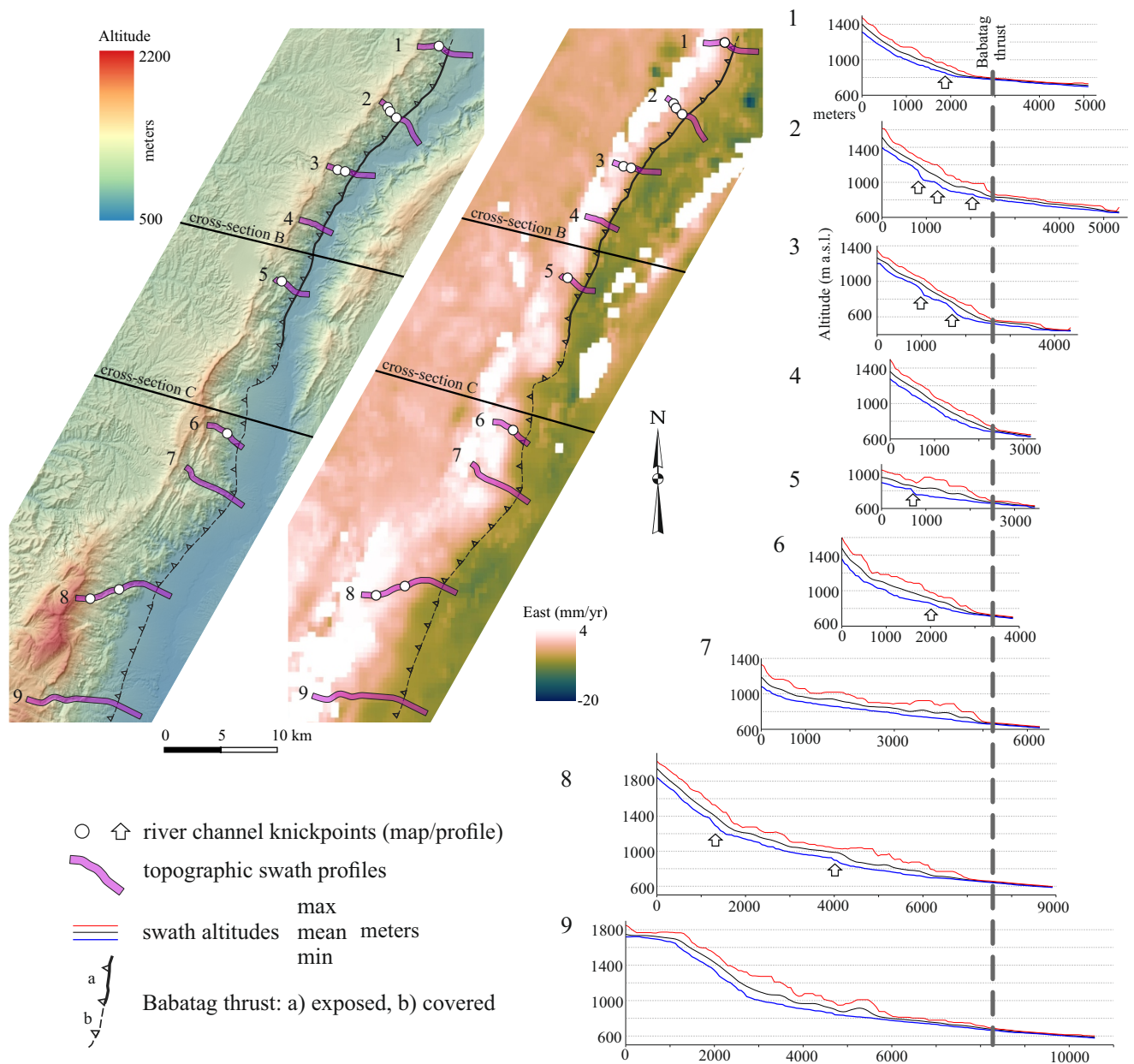


**Figure S12.** Recent activity of the Babatag thrust indicated by geomorphology. Maps plot topography, east rates, and local geology. The series of 500-m-wide swath profiles along selected stream trunks at the east-facing slopes of the Babatag anticline display knickpoints, likely indicating topographic perturbations due to slip along the Babatag thrust; due to the lack of detailed geological mapping, we cannot exclude that some of the knickpoints mark lithological changes.